WIDEBAND PHASED ARRAY ANTENNAS AND COMPACT, HARMONIC-SUPPRESSED MICROSTRIP FILTERS

A Dissertation

by

WEN-HUA TU

Submitted to the Office of Graduate Studies of
Texas A&M University
in partial fulfillment of the requirements for the degree of

DOCTOR OF PHILOSOPHY

December 2006

Major Subject: Electrical Engineering

WIDEBAND PHASED ARRAY ANTENNAS AND COMPACT, HARMONIC-SUPPRESSED MICROSTRIP FILTERS

A Dissertation

by

WEN-HUA TU

Submitted to the Office of Graduate Studies of
Texas A&M University
in partial fulfillment of the requirements for the degree of

DOCTOR OF PHILOSOPHY

Approved by:

Chair of Committee,	Kai Chang
Committee Members,	Krzysztof A. Michalski
	Kamran Entesari
	Thomas Wilheit
Head of Department,	Costas N. Georghiades

December 2006

Major Subject: Electrical Engineering

ABSTRACT

Wideband Phased Array Antennas and Compact Harmonic-Suppressed Microstrip Filters. (December 2006)

Wen-Hua Tu, B.S., National Chiao Tung University;

M.S., National Taiwan University

Chair of Advisory Committee: Dr. Kai Chang

Modern satellite, wireless communications, and radar systems often demand wideband performance for multi-channel and multi-function operations. Among these applications, phased array antennas play an important role. This dissertation covers two wideband phased array antennas, one produces linear polarization and one produces circular polarization. The main difference between these two phased array antennas is the antenna array. For the linearly polarized array, a wideband microstrip line to slotline transition is used to feed a Vivaldi antenna. For the circularly polarized array, a wideband microstrip line to parallel stripline transition is used to feed a spiral antenna. From 3 to 12 GHz, the linearly polarized beam is steered over $\pm 15^{o}$.

Since the electromagnetic spectrum is limited and has to be shared, interference is getting serious as more and more wireless applications emerge. Filters are key components to prevent harmonic interference. The harmonic signals can be suppressed by cascading additional lowpass filters or bandstop filters. A bandstop filter combining shunt open stubs and a spurline is proposed for a compact size and a deeper rejection. Two lowpass filters with interdigital capacitors and slotted ground structures are also

studied.

Harmonic suppression can also be achieved with the modification of bandpass filters. Three conventional bandpass filters with spurious passbands are investigated. The first one is a dual-mode patch bandpass filter. The second passband of the proposed filter is at $2.88f_o$, where f_o is the fundametal frequency. The second filter is an open-loop bandpass filter. Two open stubs are added to achieve high suppression in the second harmonic signal. The suppression of 35 dB at the second harmonic is obtained. For the third filter using half-wavelength open stubs, a T-shaped line is used to replace the quarter-wavelength connecting line. The T-shaped line has the same response with the connecting line in the passband. Furthermore, the T-shaped line works as a bandstop filter at the second harmonic.

Finally, a new compact slow-wave resonator and bandpass filters are presented. A simple transmission-line model is used to predict the resonant frequency. Compared with the conventional uniform half-wavelength resonator, the slow-wave resonator shows a 25% size reduction.

To my parents and my family

ACKNOWLEDGMENTS

I would like to express my deepest appreciation to Dr. Kai Chang for his support, encouragement, and guidance throughout my Ph.D. study at Texas A&M University. I also appreciate Dr. Kamran Entesari, Dr. Krzysztof A. Michalski, Dr. Henry F. Taylor, Dr. Thomas Wilheit, and Dr. Steven M. Wright for serving as members on my dissertation committee and for their helpful comments. I gratefully acknowledge Mr. Ming-yi Li and other members of the Electromagnetics and Microwaves Lab for their technical assistance, critical review on papers, and invaluable discussions.

I would like to thank my parents, brothers, and parents-in-law for their constant encouragement and support. I also thank my daughter, Deping, for her love. Finally, my sincere thanks is given to my lovely wife, Hsiao-Wan, for all her encouragement, love, and support. This work would not have been possible without their support and patience.

TABLE OF CONTENTS

Page

CHAPTER Page

LIST OF FIGURES

FIGURE Page

FIGURE Page

FIGURE Page

LIST OF TABLES

CHAPTER I

INTRODUCTION

1.1 Introduction

Modern satellite, wireless communications, and radar systems often demand the wideband performance for multi-channel and multi-function operation. Phased array antennas have proven useful for satellite communications and radar systems. The required wideband performance keeps challenging modern phased array antenna engineers. Since the beam steering is controlled by the phases on antenna elements, the phase shifter is one of the most important components. A recently published multi-line piezoelectric transducer (PET)-controlled phase shifter enables the design of a phased array with low-cost, low-loss, wideband performance, and easy fabrication. A movable dielectric substrate attached to the PET is placed on the top of the microstrip line. The dielectric substrate changes the effective dielectric constant of the microstrip line, and cause different phase shifts on the microstrip line. Antenna elements are another important components of a phased array antenna. They control the polarization of an array antenna. Two phased array antennas are studied in this dissertation. The two antenna elements are Vivaldi antennas for linear polarization and spiral antennas for circular polarization. In order to feed these antennas, two transitions from a microstrip line to a slotline and from a microstrip line to a parallel stripline are used.

Filters play important roles in many RF/microwave applications. Since the

The journal model for this dissertation is *IEEE Transactions on Microwave Theory and Techniques*.

electromagnetic spectrum is limited and has to be shared. Filters are used to select and confine signals within the assigned spectrum. Spurious passbands often occur in microstrip line bandpass filters. These spurious channels might interfere with other applications. On other hand, other applications might interfere with our application through these spurious channels. Cascading lowpass filters (LPFs) and/or bandstop filters (BSFs) is the most straightforward method to tackle this issue. A compact BSF using shunt open stubs and a spurline is proposed for a deeper and wider rejection. Two elliptic-function LPFs with an interdigital capacitor or a slotted ground structure are also proposed. Furthermore, comparisons between these two LPFs are drawn. Although cascading LPFs and/or BSFs is simple, these filters increase the insertion loss in the passband and the circuit sizes. Therefore, other methods are also proposed to suppress the harmonics. Three conventional bandpass filters (BPFs) are studied. A compact dual-mode patch BPF with right cross slot is introduced for a wider upper stopband. For the open-loop BPF, two different open stubs are included for the second harmonic suppression. For the half-wavelength open stub BPF, the quarter-wavelength connecting line is replaced by an equivalent T-shaped line, which is compact and works as a BSF at the second harmonic. Finally, a new compact slow-wave resonator is proposed. A simple transmission-line model is employed to predict the resonant frequencies. Applications to a BPF are also included.

1.2 Dissertation organization

This dissertation presents novel linearly/circularly polarized wideband phased array antenna, and couples microstrip filters. The dissertation consists of seven chapters.

Chapter II presents two wideband phased array antennas. Vivaldi antenna is used for linear polarization, and spiral antenna is used for circular polarization.

Chapter III introduces a compact BSF using two quarter-wavelength shunt open stubs and a spurline. The BSF features a compact size and a better performance.

Chapter IV describes two elliptic-function LPFs. The first one consists of a microstrip line section and an interdigital capacitor. The second LPF consists a slotted ground structure and a wide microstrip line. Transmission-line model as well as a full-wave simulation is employed in both designs. Comparisons between the two filters are also included.

Chapter V discusses three conventional BPFs with spurious passbands. Three different methods are proposed to tackle the harmonic problems.

Chapter VI introduces a new slow-wave resonator. The resonator consists of several sections of high- and low- impedance lines. Applications to a BPF are also investigated.

Chapter VII summarizes the research accomplishments in this dissertation.

CHAPTER II

WIDEBAND PHASED ARRAY ANTENNAS*

2.1 Introduction

Linearly and exponentially tapered slot antennas were first introduced in 1979 [1,2]. Since tapered slot antennas (TSAs) are printed circuit antennas, their advantages of low weight, ease of fabrication, and compatibility with microwave integrated circuits make them attractive in many applications, such as satellite and wireless communications, remote sensing, and radar. Also, TSAs can produce a symmetric beam in both E- and H-plane by correctly choosing the shape, length, dielectric thickness, and dielectric constant [3]. Furthermore, it is a traveling structure that makes it suitable for the transmission of the pulse signal without much dispersion in the time domain [4], and TSA becomes a good candidate for ultra wideband systems that use narrow pulse to transmit data. Common TSAs are of linear, exponential, or linear-constant width profiles. Exponential TSAs are also referred as Vivaldi antennas producing linear polarization.

TSAs can only produce linear polarization. For applications that the polarization of the transmitting antenna is unknown or for a moving target, circularly polarized receiving antennas are required. Spiral antenna is a good candidate for wideband circularly polarized applications [5]- [8]. Classical shapes of spiral antennas include the

---

* Parts of this chapter are reprinted, with permission, from W.-H. Tu, S.-G. Kim and K. Chang, " Wideband microstrip-fed tapered slot antennas and phased array," to appear in *International Journal of RF and Microwave Computer-Aided Engineering*. © Wiley InterScience.

equiangular geometries [5] and the logarithmically geometries [8]. Theoretically, spiral antennas have an infinite bandwidth, but it is the feeding structure and the truncation that limit the bandwidth. The lowest frequency of the operation frequency occurs when the total arm length is comparable to the wavelength. On the hand, the highest operation frequency is affected by the precision of the feed structure. Furthermore, the polarization is controlled by the arm length. For low frequency, the arm length is small compared to the wavelength and the radiated field is linearly polarized. As the frequency increases, the wave becomes elliptically polarized and eventually achieves circular polarization.

The phase shifter is another important component for a phased array. Recently, a PET-controlled multi-line phased shifter was reported [9]. It features several advantages: low power consumption of less than 1 mW, high power handling capability, low dc control voltage of 60 V in comparison to that of a ferrite plate, smaller sizes, no matching circuit required, and wider operation bandwidth due to a true time-delay type of phase shifting.

In this chapter, two wideband phased array antennas are developed. One antenna produces linear polarization and the other one produces circular polarization.

2.2 Wideband linearly polarized phased array antenna

A. Microstrip line to slotline transition

The phased array antenna is designed to operate from 3 to 12 GHz. Therefore, every component is designed to operate within the above bandwidth. Fig. 1 shows the configuration and equivalent circuit of a microstrip line to slotline transition.

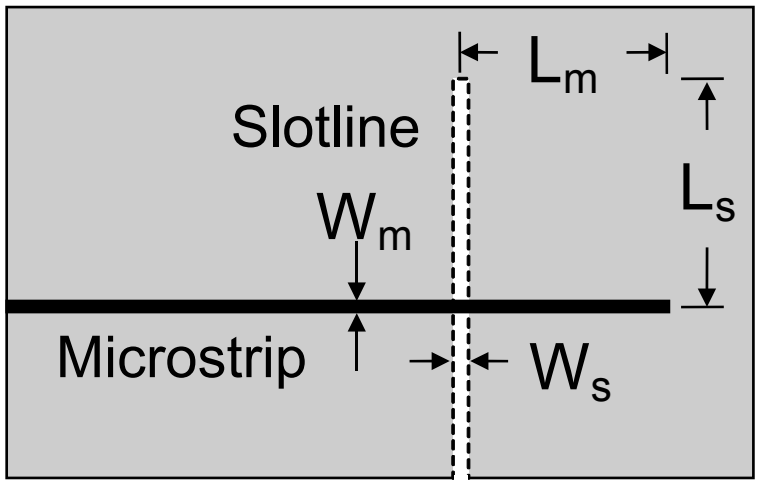

(a)

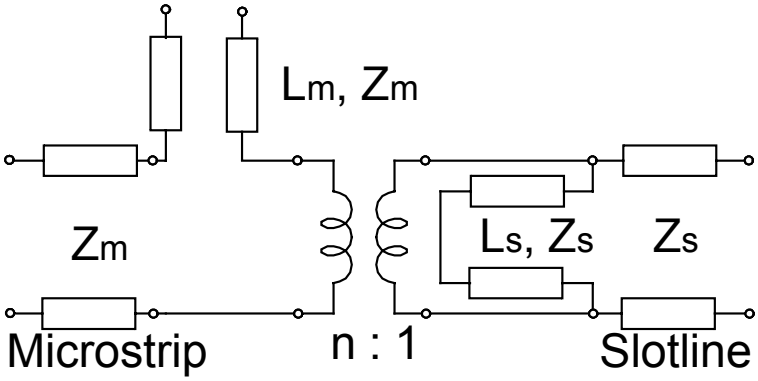

(b)

Fig. 1. Microstrip line to slotline transition (a) configuration and (b) equivalent circuit.

The microstrip line and slotline are on the different sides of the substrate. At a given frequency, an impedance matching can be obtained by selecting [10]

$$Z_m = n^2 Z_s \tag{1}$$

where

$$n = \cos\left(2\pi \frac{h}{\lambda_0} u\right) - \cot q_0 \sin\left(2\pi \frac{h}{\lambda_0} u\right)$$

$$q_0 = 2\pi \frac{h}{\lambda_0} u + \tan^{-1}\left(\frac{u}{v}\right)$$

$$u = \sqrt{\varepsilon_r - \left(\frac{\lambda_0}{\lambda_s}\right)^2}$$

$$v = \sqrt{\left(\frac{\lambda_0}{\lambda_s}\right)^2 - 1}$$

where h is the substrate thickness; ε_r is the relative dielectric constant of the substrate; λ_0 is the free space wavelength at the given frequency; λ_s is the guided wavelength of the slotline at the given frequency; Z_m and Z_s are the characteristic impedances of the microstrip line and slotline, respectively. Since the slotline characteristic impedance increases as its width (W_s) increases, the slotline width should be as small as possible for a low characteristic impedance and the ease of impedance matching. However, etching a very thin slot will increase the fabrication error. Therefore, W_s is first chosen as 0.2 mm considering the fabrication tolerance of the wet etching facility, and then Z_s and Z_m are determined accordingly. In order to achieve a wider bandwidth, two fan stubs as well as a multi-section microstrip impedance transformer [11] is used. Fig. 2 shows the configuration of the wideband transition. The transition is built on a 20-mil RT/Duroid 5880 with a dielectric constant of 2.2. Fig. 3 shows the simulated and measured results. The simulation is carried out by a full-wave electronmagnetic simulator IE3D[*]. From 1.8 to 14.5 GHz, the return loss is better than 10 dB, and the insertion loss excluding the connector's losses is less than 3.1 dB. The insertion loss increases as frequency increases

[*] IE3D version 10.2, Zeland Software Inc., Fremont, CA, 2004.

from 1 dB at 1.8 GHz to 3.1 dB at 14.5 GHz. Due to multiple reflections of the connectors, measured result shows more ripples in the return loss, compared to the simulation result.

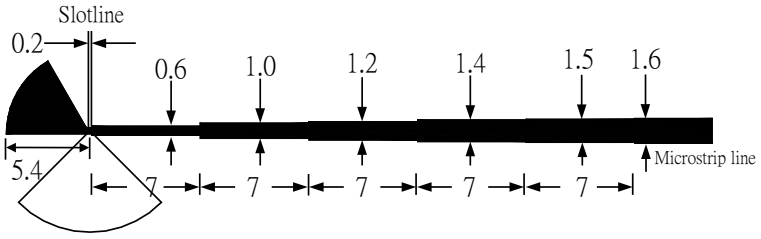

Fig. 2. Transition with multisection matching transformer [unit : mm].

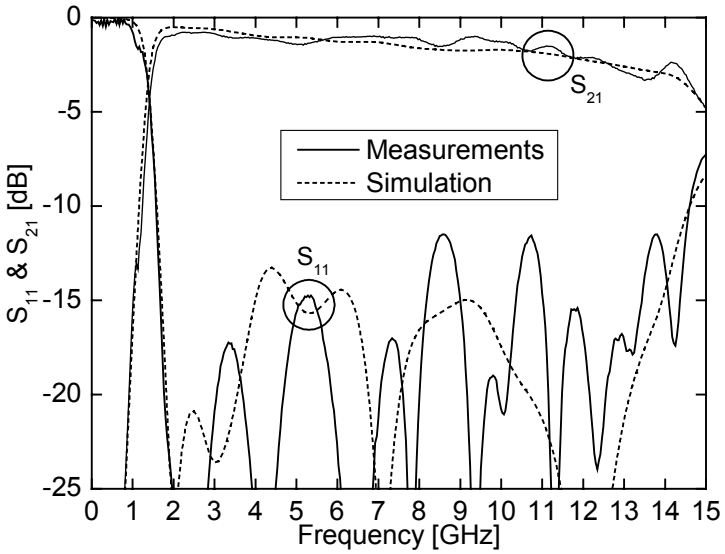

Fig. 3. Measured and simulated S-parameters of the back-to-back transition with substrate of dielectric constant of 2.2.

B. Vivaldi antenna

With the wideband transition, the full-wave electromagnetic simulator software CST Microwave Studio* is used to determine the optimal taper factor *R*, the length *L*, and the aperture width *W*. The dimensions of the Vivaldi antenna shown in Fig. 4 are: *L* = 150 mm (1 λ_0), *W* = 100 mm (0.67 λ_0), *D* = 0 mm, and *R* = - 0.15, where λ_0 is free space wavelength at 2 GHz. The exponential taper is chosen for its wideband performance. The slot flare is determined by a taper factor *R* according to the equation [12]:

$$y = c_1 e^{Rx} + c_2 \qquad (2)$$

where $c_1 = \frac{y_2 - y_1}{e^{Rx_2} - e^{Rx_1}}$, $c_2 = \frac{y_1 e^{Rx_2} - y_2 e^{Rx_1}}{e^{Rx_2} - e^{Rx_1}}$. The start and end points of the flare determine the constants c_1 and c_2. In this case, the coordinate of start point (x_1 , y_1) is (0.1 , 0), and that of the end point (x_2 , y_2) is (50 , 150) with the origin at the center of the slotline with W_s = 0.2.

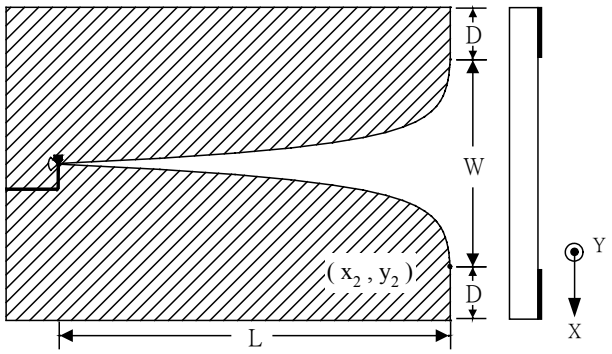

Fig. 4. Vivaldi antenna.

* Microwave Studio version 4, CST, Darmstadt, Germany, 2003.

Fig. 5 shows the simulated and measured return loss of the Vivaldi antenna. From 1.8 to 15.2 GHz, the return loss is better than 10 dB. The patterns are shown in Fig. 6. The antenna gain increases monotonically versus frequency and varies from 5 to 15.6 dBi. The cross-polarization level is more than 13 dB below the co-polarization level.

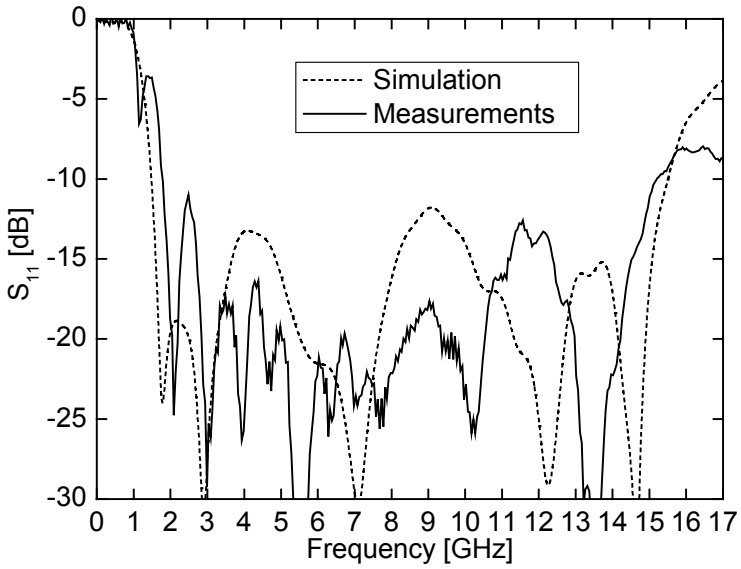

Fig. 5. Measured and simulated return loss of the Vivaldi antenna.

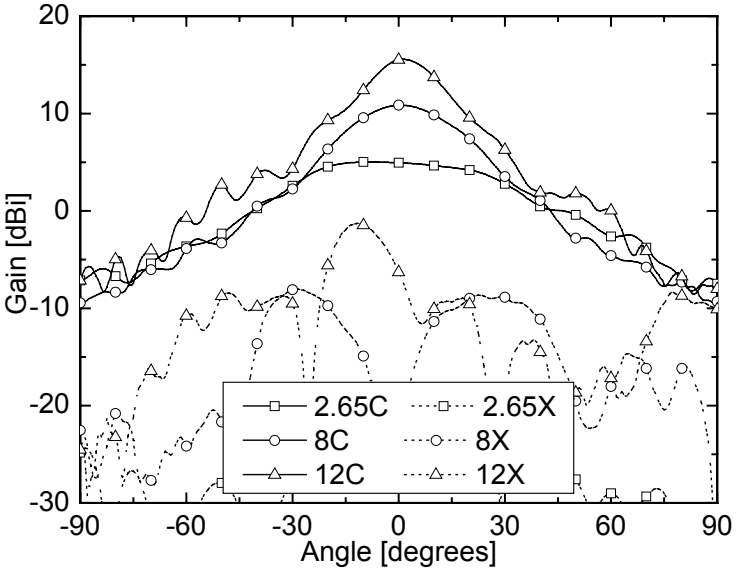

(a)

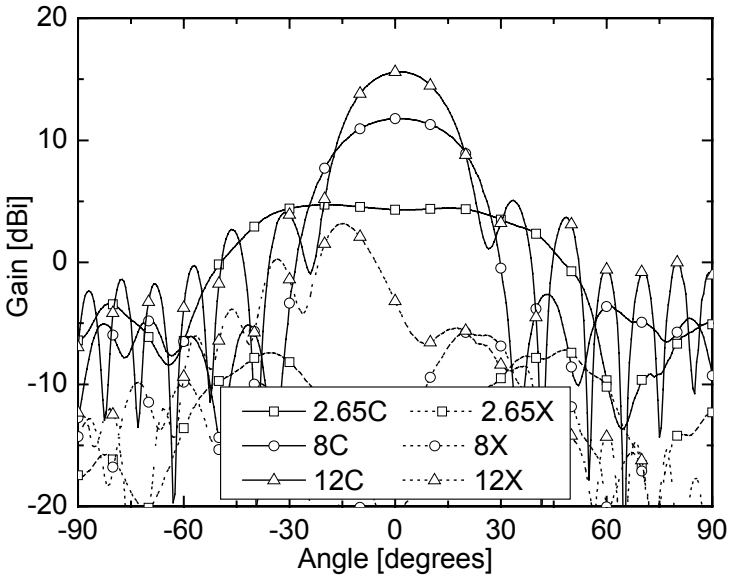

(b)

Fig. 6. Measured antenna patterns with substrate of dielectric constant = 2.2 at 2.65, 8, and 12 GHz. C represents co-polarization and X represents cross-polarization.

C. Phased array antenna

Fig. 7 shows the configurations of the 1 x 4 H-plane linearly polarized phased array. The H-plane array is chosen since it is easier to have close element spacing in a H-plane array. The phased array antenna consists of a four-way power divider using five-section Chebyshev transformers [11], a PET-controlled phase shifter [9], and an 1x4 H-plane Vivaldi antenna array. SMA connectors are used to connect the power divider, phase shifter, and antenna array. The antenna element spacing is chosen as 18 mm (0.72 λ_0 at 12 GHz and 0.12 λ_0 at 2 GHz) considering the connector size, grating lobes, and steering angle. To decrease the cross-polarization from the radiation of feed line discontinuities, the feed lines of the upper and lower two antennas are face-to-face in mirror arrangement, and the radiation from the feed lines will cancel out each other at the cross-polarization direction [13], [14].

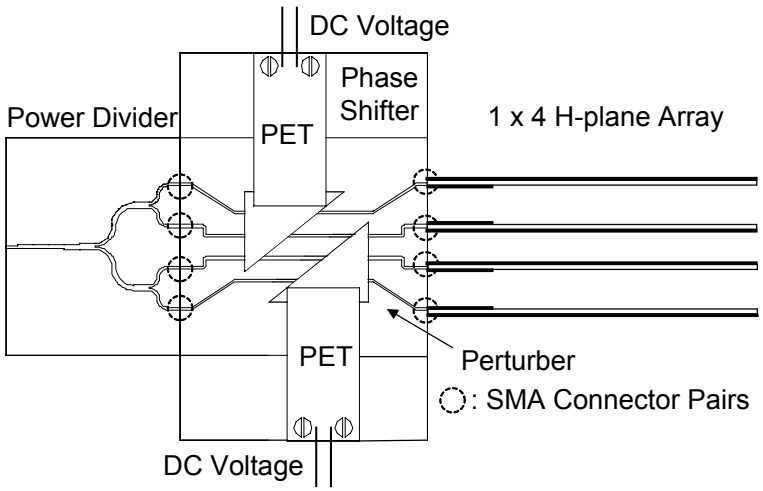

(a)

Fig. 7. Configuration of the linearly polarized phased array antenna (a) top view and (b) 3-D view.

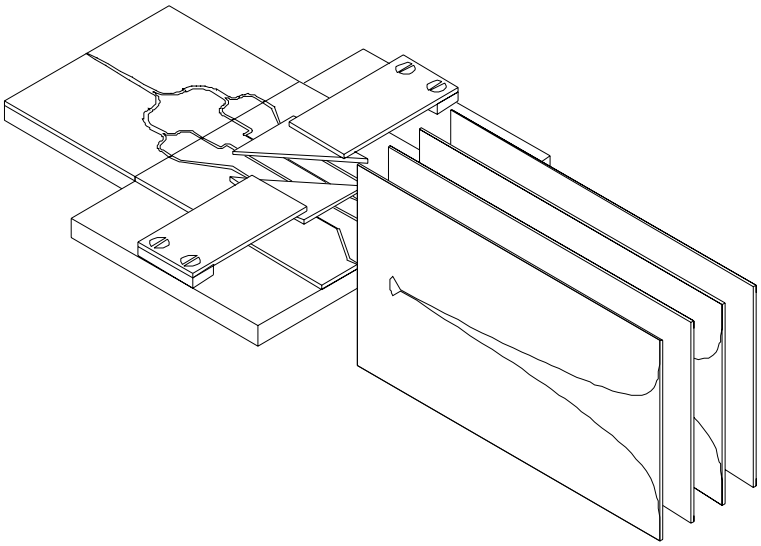

(b)

Fig. 7. Contiuned

The power divider and phase shifter are built on 15-mil RT/Duroid 5880 (dielectric constant = 2.2) substrates, and a 50-mil RT/Duroid 6010.2 (dielectric constant = 10.2) substrate is used as the perturber for the phase shifter. The power divider is designed to cover the whole operation bandwidth of the antenna and shows a measured input return loss of better than 10 dB from 1.2 to 15.2 GHz. The multi-line PET-controlled phase shifter has the advantages of low power consumption less than 1 mW, low DC control voltage less than 55 V, wide operation bandwidth due to the true time-delay type of phase shifting, high power handling capability, and no requirement of impedance matching circuits [9]. The differential phase $\Delta\phi$ is determined by the coverage length of the perturber, effective relative permittivity of perturbed and unperturbed microstrip line given by [13]:

$$\Delta\phi = L\frac{2\pi}{\lambda_0}\left(\sqrt{\varepsilon_{eff}(f)} - \sqrt{\varepsilon'_{eff}(f)}\right) \quad (3)$$

where L is the coverage length under the perturber, λ_0 is the free space wavelength, and $\varepsilon_{eff}(f)$ and $\varepsilon'_{eff}(f)$ are the effective relative permittivity of the unperturbed and perturbed microstrip lines, respectively. Therefore, the lengths of perturber over each microstrip line are designed to be 1.5, 3, and 4.5 cm to achieve a progressive phase shift of 90^o at 12 GHz.

Fig. 8 shows the measured return loss of the phased array with PET's external voltages of 0, 30, and 55 volts. The return loss is better than 10 dB from 1.6 to 15 GHz for all cases. Fig. 9 shows the steered beam patterns measured at 3, 8, and 12 GHz. The total gain of the phased array varies from 9 to 17 dBi. The beam is steered over $\pm 15^o$ in the H-plane using the PET-controlled phase shifter with the external voltage of 55 volts. The broadside and scanned cross-polarization levels are more than 20 dB below the co-polarization levels.

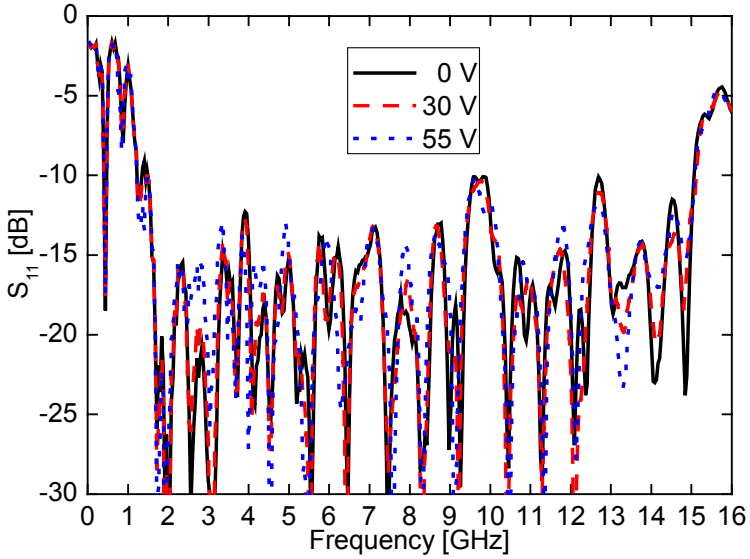

Fig. 8. Measured return loss of the 1x4 H-plane Vivaldi phased array.

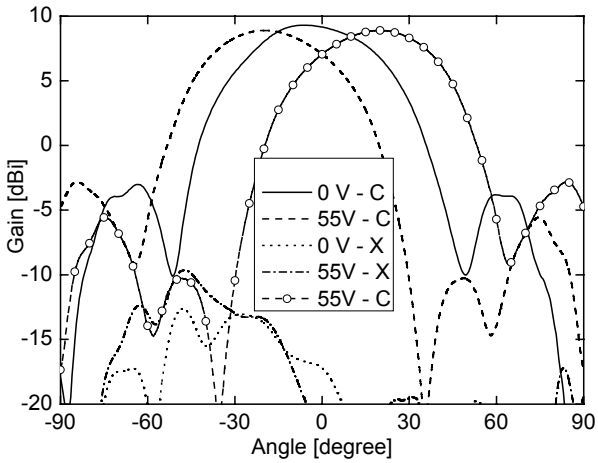

(a)

Fig. 9. Measured H-plane beam steering patterns at (a) 3 GHz (b) 8 GHz and (c) 12 GHz. C represents co-polarization, X represents cross-polarization, and circular marker is for opposite beam scanning.

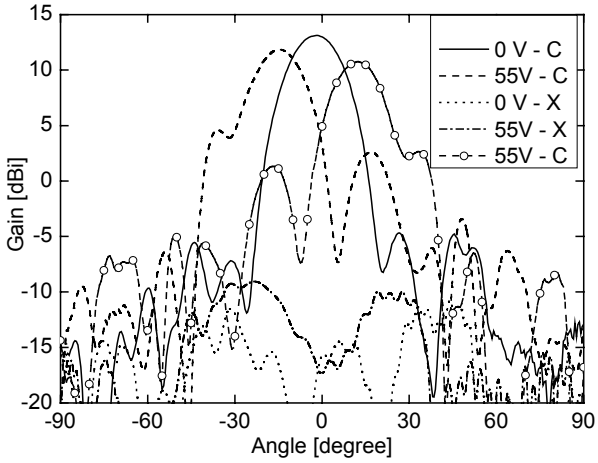

(b)

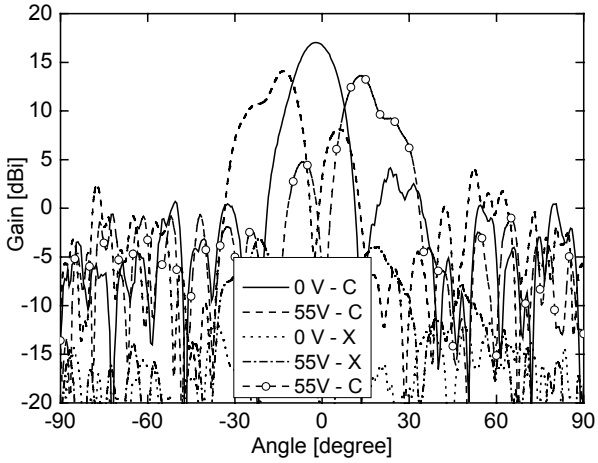

(c)

Fig. 9. Continued.

Since the single element H-plane pattern becomes narrower as the frequency increases, the steering pattern gain at 12 GHz drops by 3.6 dB compared with the broadside pattern. On the other hand, for a smaller steering angle of 11^{o} with the external voltage of 30 volts, the gain drops only by 1 dB. Fig. 10 shows the comparison of measured beam-steering patterns and two simulated beam-steering patterns. For case #1,

the patterns are calculated by multiplying the measured single element H-plane patter with the measured amplitude and phase shifts of the power divider and phase shifter. For case #2, the patterns are calculated by multiplying the measured single element H-plane patterns with ideal amplitude (uniformly excited sources) and phase (22.5^o at 3 GHz, 60^o at 8 GHz, and 90^o at 12 GHz) to achieve the steering angle of 15^o. The antenna gains of case #2 are higher than those of case #1 and those of the measured results due to the imperfect amplitude distributions, extra losses from power divider and phase shifter (1 dB at 3 GHz, 3 dB at 8 GHz, and 4 dB at 12 GHz), and imperfect progressive phase shifts. From Fig. 10, the patterns of case #1 agree well with the measured patterns. The measured patterns could be further improved by additional optimization process and better fabrication tolerance.

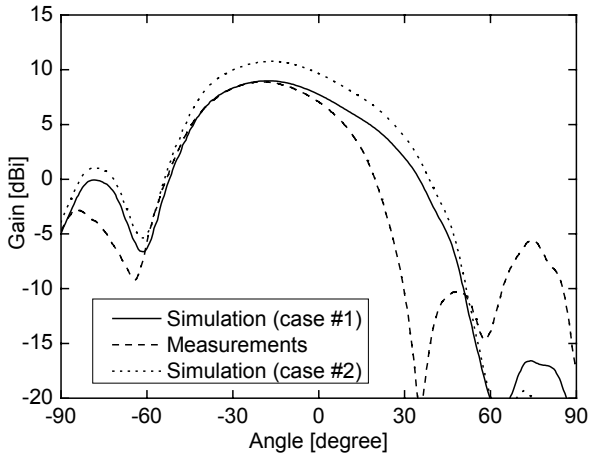

(a)

Fig. 10. Simulated and measured beam-steering patterns with an external voltage of 55 volts at (a) 3 GHz (b) 8 GHz and (c) 12 GHz.

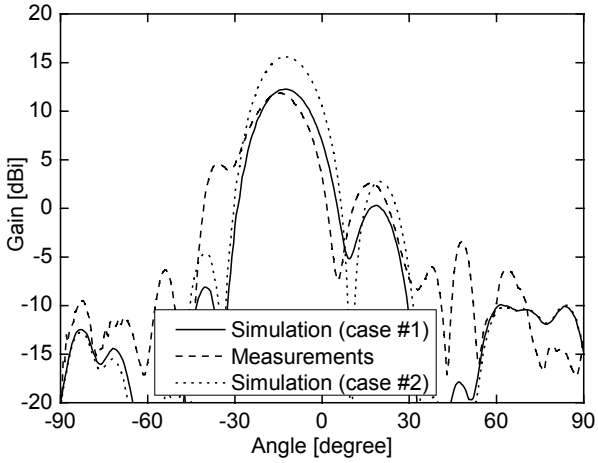

(b)

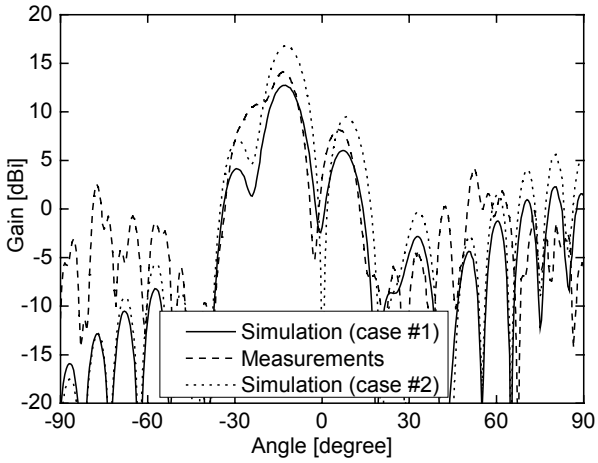

(c)

Fig. 10. Continued.

2.3 Wideband circularly polarized phased array antenna

A. Microstrip line to parallel stripline transition

Fig. 11 shows the configuration of a back-to-back microstrip line to parallel stripline transition [15]. The ground plane of the microstrip line is removed circularly. Both the microstrip line and the parallel stripline are of 50 ohm. The dimensions of the transition are: W_m = 2.5 mm, R = 15 mm, and W_{ps} = 0.8 mm. Fig. 12 shows the simulated

and measured results of the back-to-back transition. The simulation is carried out by IE3D* to optimize the radius *R*. The transition is built on a 20-mil RT/Duroid 5880 (dielectric constant = 2.2) substrate.

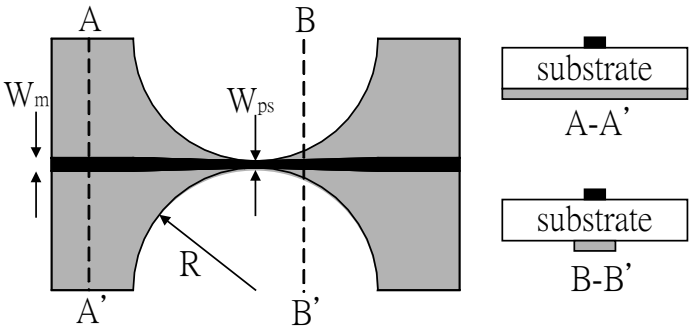

Fig. 11. Configuration of a back-to-back microstrip line to parallel stripline transition.

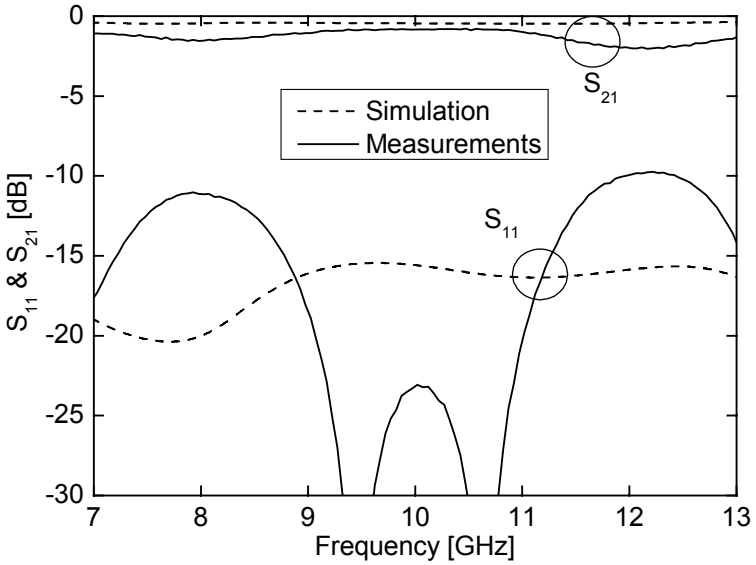

Fig. 12. Simulated and measured results of a back-to-back microstrip line to parallel stripline transition.

* IE3D version 10.2, Zeland Software Inc., Fremont, CA, 2004.

From 8 to 12 GHz, the return loss is better than 10 dB and the insertion loss is less than 2 dB.

B. Spiral antenna

Fig. 13 shows the configuration of a microstrip-parallel stripline-fed spiral antenna. The two conductors of the parallel stripline are connected to the two arms of the spiral antenna at the center by using epoxy. The spirals are designed by the following equations: $r_1 = r_0 e^{a\theta}$ and $r_2 = r_0 e^{a(\theta-\theta_0)}$, where r_1 and r_2 are the outer and inner radius of the spirals, respectively, a is the growth rate, θ is the angular position, and θ_0 controls the arm width. The parameters are: r_0 = 2 mm, a = 0.221, and $\theta_0 = 90^o$. The arm length is 43.4 mm. For low frequency, as the arm length is small compared to the wavelength, the antenna is linearly polarized. As the frequency increases, it becomes elliptically polarized and then eventually circularly polarized [5]. The spirals are built on a 20-mil RT/Duroid 5880 substrate. The spirals are of two turns for each arm.

Fig. 13. Configuration of a spiral antenna. (a) top view and (b) front view.

Fig. 14 shows the measured return loss of the four spiral antennas for the H-plane array. Minor discrepancy is observed. The measured return loss is better than 7.5 dB from 6.85 to 11.9 GHz. The return loss can be improved with a finer assembly tolerance for the vertical structure from parallel strip to spiral antenna. Fig. 15 shows the measured antenna patterns at 9, 10, 11, and 12 GHz.

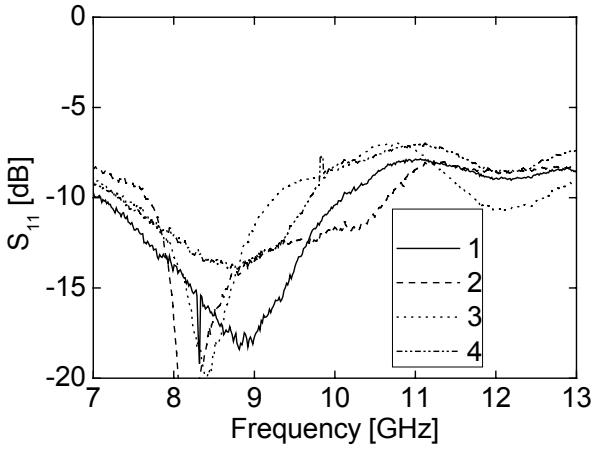

Fig. 14. Measured return loss of a spiral antenna.

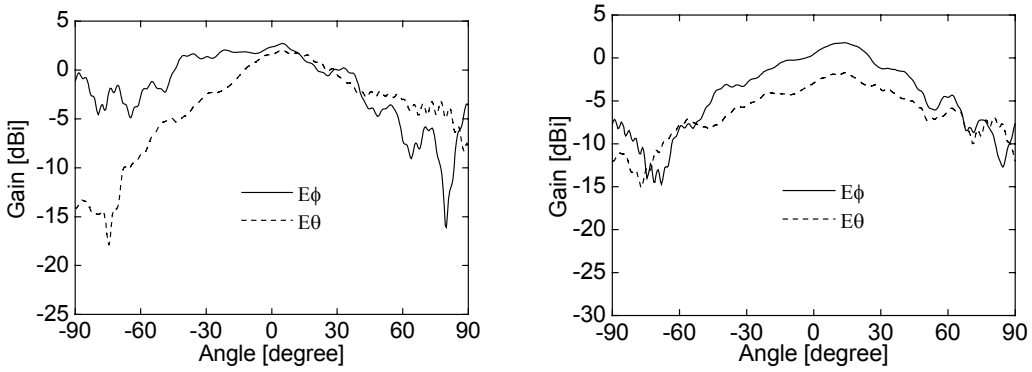

(a) (b)

Fig. 15. Measured patterns of a spiral antenna at x-z plane. (a) 9 GHz (b) 10 GHz (c) 11 GHz and (d) 12 GHz.

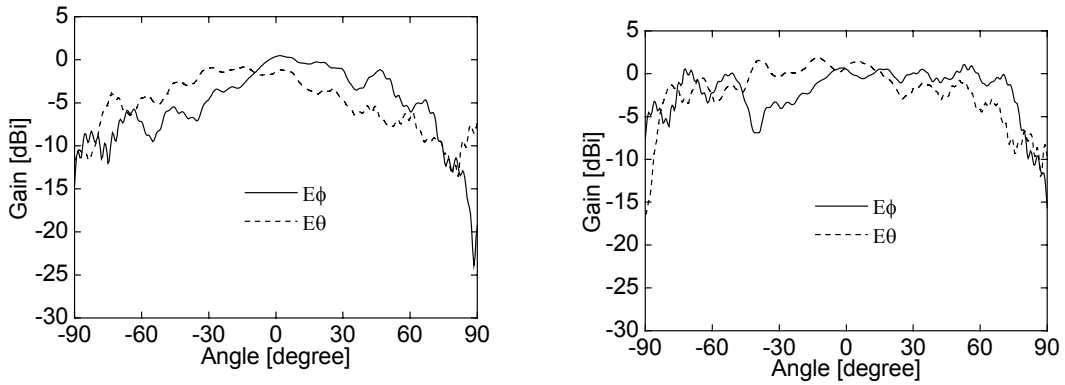

(c) (d)

Fig. 15. Continued.

Fig. 16 shows the axial ratio. The antenna shows a good CP characteristic with its axial ratio less than 1 dB from 7.5 to 9.5 GHz and less than 3 dB from 7 to 11.5 GHz.

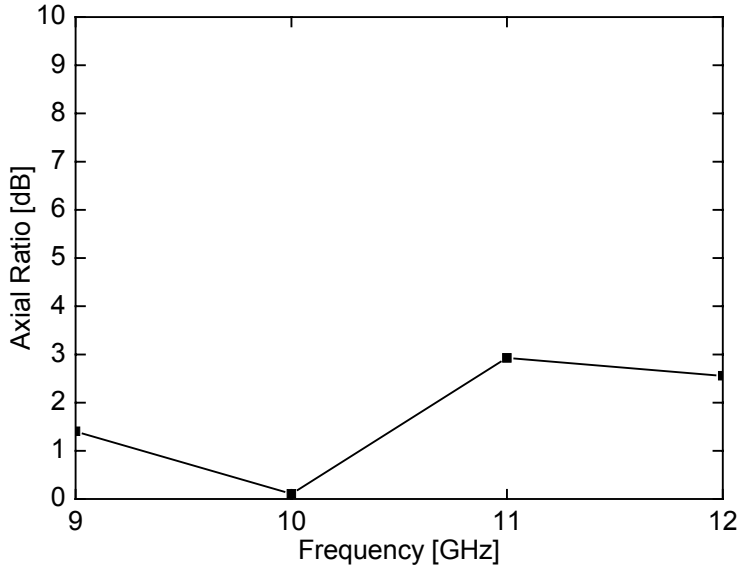

Fig. 16. Axial ratio of a spiral antenna.

C. Phased array antenna

Fig. 17 shows the configuration of the circularly polarized wideband phased array antenna. The phased array antenna consists of a power divider, a phase shifter, and an 1 x 4 H-plane Spiral antenna array. The power divider and the phase shifter are the same with those used in previously linearly polarized phased array antenna.

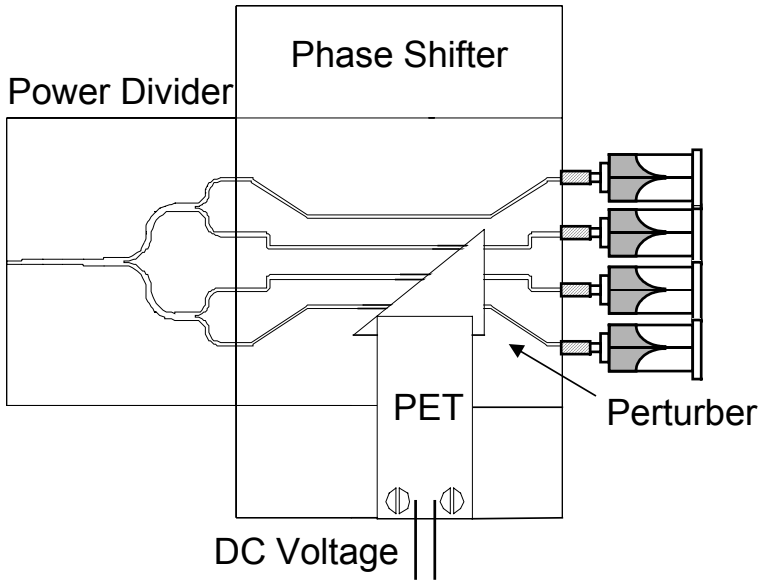

Fig. 17. Configuration of the circularly polarized phased array antenna.

Fig. 18 shows the measured return loss of the circularly polarized phased array antenna. The return loss is better than 7.5 dB from 7 to 13 GHz. With different dc voltages, the return loss change slightly. Fig. 19 shows the measured antenna patterns of the phased array antenna at 9, 10, 11, and 12 GHz. Some discrepancies are observed due to fabrication and assembling tolerance. These radiation patterns could be further improved by additional optimization process and finer fabrication tolerance.

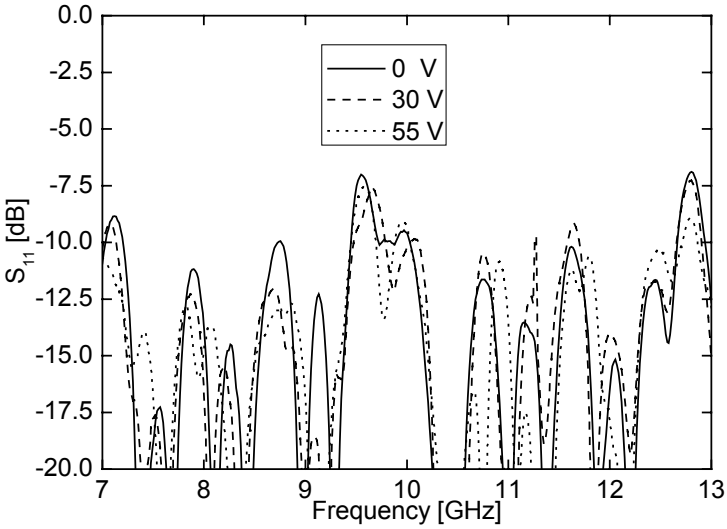

Fig. 18. Return loss of the circularly polarized phased array antenna.

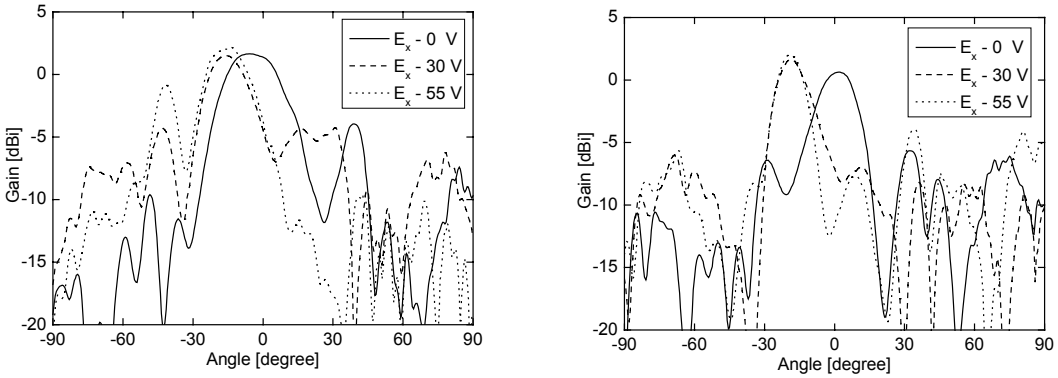

Fig. 19. Measured patterns of a phased antenna at x-z plane. (a) 9 GHz (b) 10 GHz (c) 11 GHz and (d) 12 GHz.

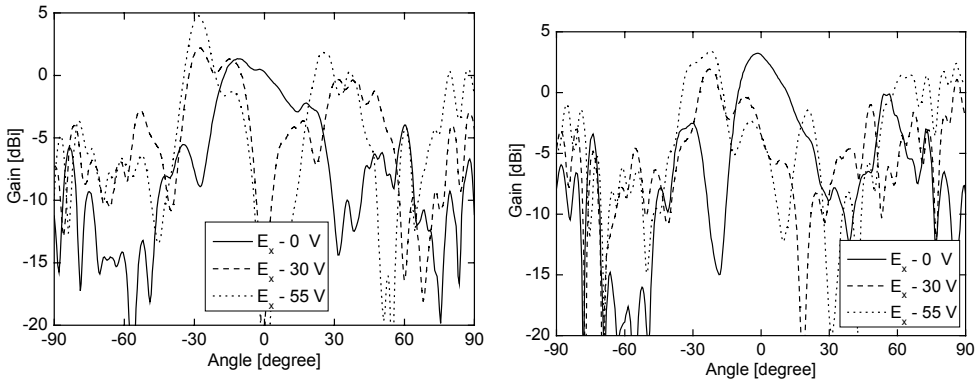

(c) (d)

Fig. 19. Continued.

2.4 Conclusions

In this chapter, a linearly polarized phased array antenna and a circularly polarized phased array antenna are studied. Several components are investigated, such as the microstrip line to slotline transition, the microstrip line to parallel stripline transition, the PET-controlled phased shifter, the Vivaldi antenna, and the spiral antenna. These phased array antennas should find many applications in radar and satellite communication systems.

CHAPTER III

COMPACT MICROSTRIP BANDSTOP FILTER USING OPEN STUB AND SPURLINE*

3.1 Introduction

Bandstop filters have found many applications in microwave/millimeter-wave systems to reject undesired frequencies. A shunt quarter-wavelength (at fundamental frequency) open stub located at the output port of a doubler provides a low impedance level to reject the unwanted fundamental frequency and a high impedance level to let the desired second harmonic pass through [16]. A diplexer using periodic stubs to reject the unwanted frequencies has a passband between two adjacent stopbands [17]. A dual-behavior resonator consists of two parallel open stubs of different lengths. Each stub has its own stopbands, and then a passband is obtained between two adjacent stopbands [18]. Furthermore, a bandstop filter can be used as a RF choke to maintain a transmission for direct current and to choke off RF transmission over its stopbands [19].

In this chapter, microstrip bandstop filters using shunt open stubs and spurlines are presented. Basically, by cascading more identical open-stub sections of an open-stub filter, a deeper rejection and a wider rejection bandwidth can be achieved at the expense of increasing circuit size and insertion loss. Spurline bandstop filter [20], [21] with its

---

inherently compact characteristics can be embedded between two adjacent shunt open stubs to introduce another attenuation pole which achieves a better rejection performance without any penalty of increasing size. Therefore, a bandstop filter using the combination of open stubs and spurline is proposed. Furthermore, this bandstop filter can be used to suppress the second harmonic of an open-loop ring bandpass filter [22], [23] or any other type of bandpass filter. The proposed bandstop filter shows a 40 dB rejection improvement at the second harmonic.

3.2 Bandstop filter using open stubs and spurline

Fig. 20 shows the configurations of the bandstop filters using two shunt open stubs, a spurline, and the combination of two open stubs and a spurline. As shown in Fig. 20(a), the two stubs are $\lambda_g/4$ apart, and the stub length is $\lambda_g/4$, where λ_g is the guided wavelength of the microstrip line at the center frequency. The spurline filter is consisted of a $\lambda_g/4$ L-shape thin slot embedded in microstrip line. Basically, in order to obtain a deeper rejection and a wider stopband of the open-stub filter, more open stubs should be employed. However, it would also increase the circuit size and the insertion loss [20]. On the other hand, spurline filter is suitable only for moderate rejection bandwidth (about 10%) applications. To overcome these problems, a bandstop filter using a spurline sandwiched between two open stubs is proposed as shown in Fig. 20(c). Compared with Fig. 20(a), the additional spurline shown in Fig. 20(c) introduces another attenuation pole to obtain a deeper rejection and a wider stopband without increasing the circuit size. In addition, compared with Fig. 20(b), the proposed filter provides a wider

rejection bandwidth because of introducing the two open stubs that are suitable for wideband applications [19].

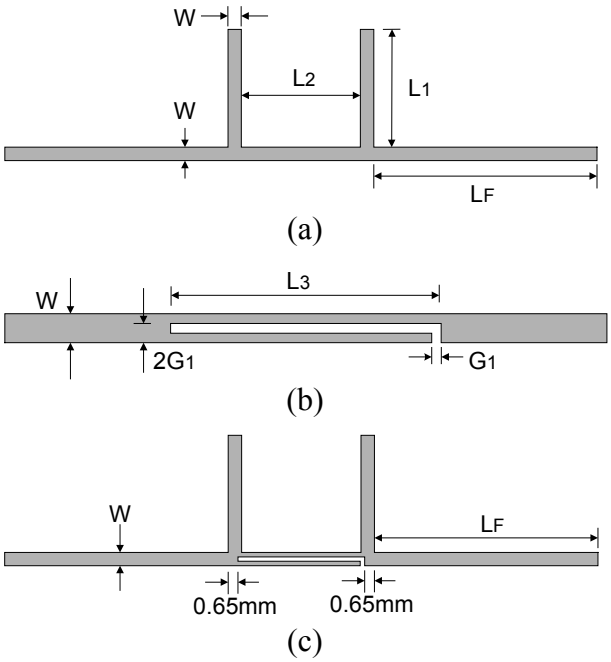

Fig. 20. Configurations of bandstop filters using (a) open stubs (b) spurline and (c) combination of open stubs and spurline.

All these filters are built on 25-mil RT/Duroid 6006 (dielectric constant = 6.15) substrates, and the simulation is performed by a commercial full-wave electromagnetic simulator IE3D*. Both of the two conventional filters are designed with the center frequency of 4.5 GHz. The optimized dimensions for parameters are: L_1 = 7.9 mm, L_2 = 8 mm, L_3 = 8.5 mm, G_1 = 0.3 mm, and W = 0.9 mm for a 50 ohm line. L_F is chosen as 15 mm for the convenience of measurements. Fig. 21 shows the simulated and measured

* IE3D version 10.2, Zeland Software Inc., Fremont, CA, 2004.

results. The measured 20-dB rejection band of the open-stub, the spurline, and the proposed filters are 3.9-5 GHz, 4.3-4.5 GHz, and 3.7-5.4 GHz, respectively, and the proposed filter has the deepest rejection level of 61 dB among these three filters. Under the circumstance of the same circuit sizes, the proposed filter shows a better rejection than the traditional open-stub filter. Furthermore, the proposed filter has a wider stopband than the spurline filter.

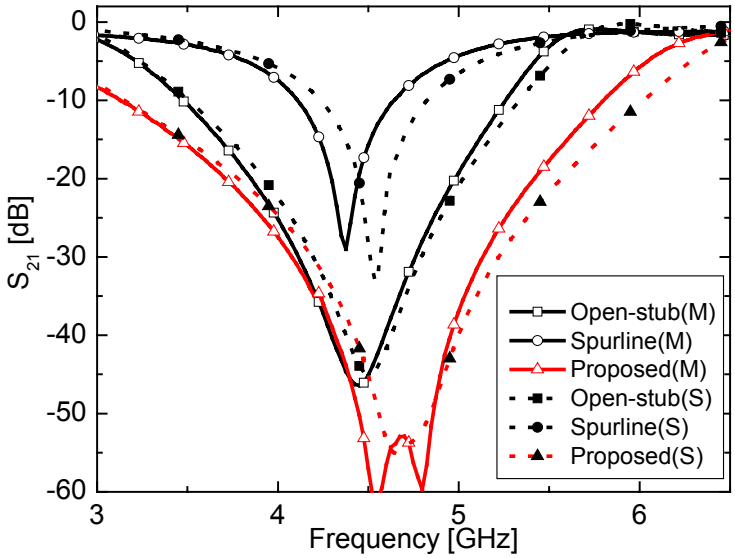

Fig. 21. Simulated and measured insertion loss of bandstop filters. M represents measurements, and S represents simulation.

3.3 Bandpass filter with second harmonic suppression

Fig. 22 shows the configurations of an asymmetric-fed open loop ring bandpass filter [23] with and without the bandstop filters that are used to suppress the second harmonic of the bandpass filter. The dimensions of these filters are: L_1 = 8.7 mm, L_2 =

8.4 mm, L_3 = 8.5 mm, L_4 = 13.95 mm, L_5 = 19.75 mm, L_6 = 11.6 mm, G_1 = 0.3 mm, G_2 = 0.5 mm, G_3 = 0.4 mm, and W = 0.9 mm.

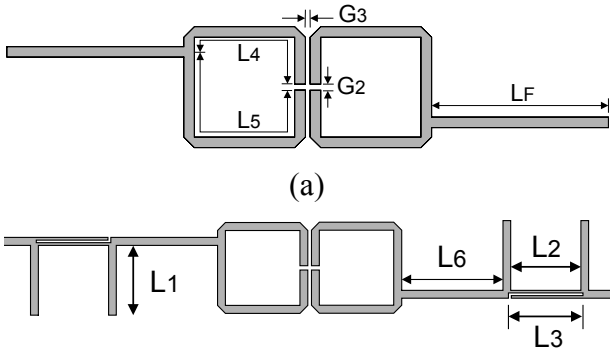

Fig. 22. Configurations of filters using two open-loop ring resonators (a) filter only and (b) filter with proposed bandstop filters.

Fig. 23 shows the measured insertion loss of the bandpass filter only and bandpass filters with the proposed bandstop and the open-stub filters.

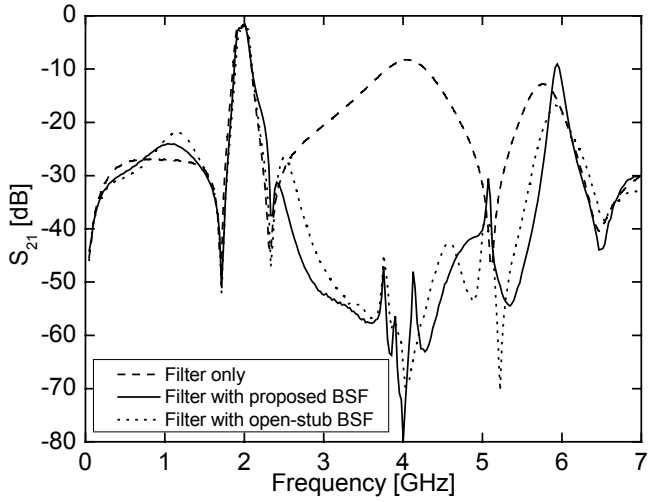

Fig. 23. Measured insertion loss of bandpass filter with and without bandstop filters.

The center frequency of the bandpass filter is 1.95 GHz, and the second harmonic at 3.9 GHz is suppressed from 8 dB without bandstop filter to 48 dB with the bandstop filter. An improvement in suppression of 40 dB is achieved. Furthermore, the proposed bandstop filter shows a better suppression performance than the conventional open-stub filter. Fig. 24 shows the measured and the simulated results of the ring bandpass filter with the bandstop filters. The simulated return loss is better than 20 dB. The measured passband ranges from 1.9 to 2 GHz. The return loss is better than 10 dB, and the insertion loss including connector loss is less than 2.4 dB. The difference between simulation results and measured results is mainly due to fabrication tolerance. From 2.3 to 5.7 GHz, the suppression is better than 30 dB, and when below 1.8 GHz, the suppression is better than 24 dB.

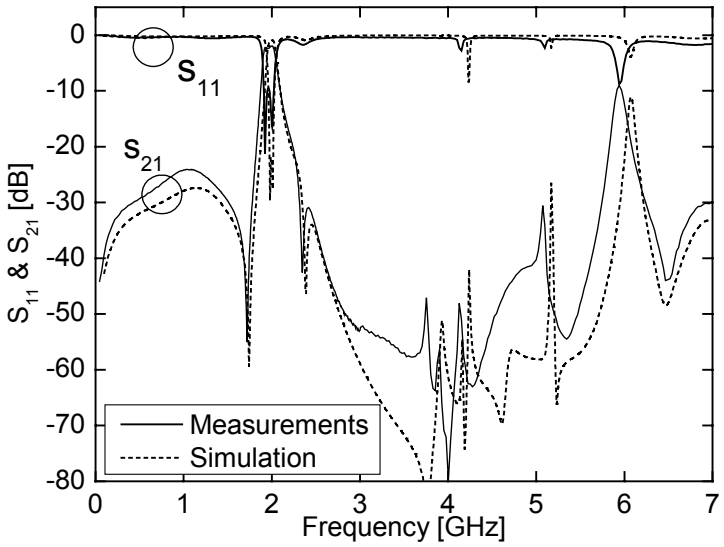

(a)

Fig. 24. Simulated and measured results of bandpass filter with bandstop filters (a) whole frequency range and (b) near passband frequency.

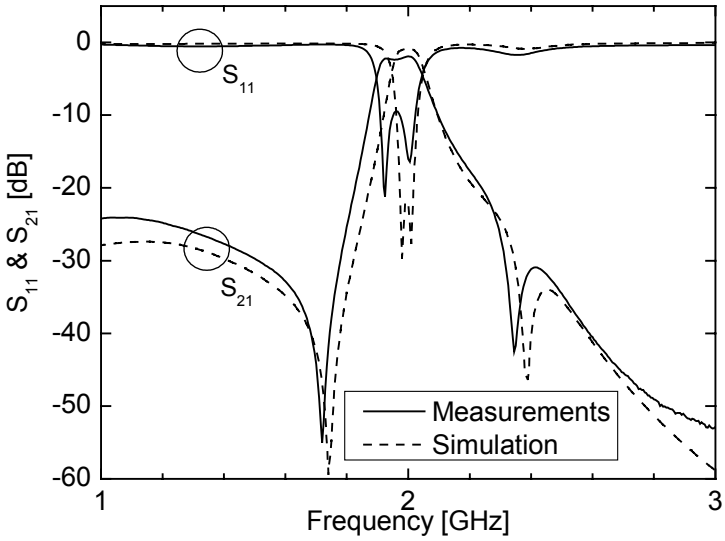

(b)

Fig. 24. Continued.

3.4 Conclusions

By applying the inherently compact characteristics of spurline, a bandstop filter using the combination of open stubs and a spurline is proposed. The proposed bandstop filter shows a much deeper rejection and wider stopband than the conventional open-stub bandstop filter without increasing the circuit size. This filter is also used to suppress the second harmonic of an open-loop ring bandpass filter with a center frequency of 1.95 GHz. The suppression is better than 30 dB, from 2.3 to 5.7 GHz.

CHAPTER IV

MICROSTRIP ELLIPTIC-FUNCTION LOWPASS FILTERS USING DISTRIBUTED ELEMENTS OR SLOTTED GROUND STRUCTURE*

4.1 Introduction

In many communication systems, low-pass filters are the key components to suppress the undesired harmonics and spurious signals. The conventional stepped-impedance filters, however, can only provide a gradual cutoff frequency response [11]. In order to achieve a sharp cutoff frequency response, more sections are needed, but more sections will also increase the insertion loss in the passband and the circuit size. Recently, semi-lumped low-pass filters [24] have been reported with a sharp cutoff frequency response due to the usage of the lumped capacitors. Unfortunately, soldering lumped components not only introduces parasitics but also makes manufacturing repeatability difficult to maintain. Low-pass filters using coupled lines [25] or stepped-impedance hairpin resonators [26] have finite attenuation poles in the cutoff frequency band. However, because the capacitance of the coupled lines is too small, the finite attenuation pole cannot be located close to the passband. Consequently, the cutoff frequency response is gradual. The low-pass filter [27] with a microstrip line

---

* Parts of this chapter are reprinted, with permission, © 2006 IEEE from W.-H. Tu and K. Chang, "Microstrip elliptic-function lowpass filters using distributed elements or slotted ground structure," *IEEE Trans. Microw. Theory Tech.*, vol. 54, no. 10, pp. 3786-3792, Oct. 2006.

section and an interdigital capacitor has been proposed for sharp rejection. But the analysis is focused on locating the attenuation poles for suppressing the specific harmonics and spurious signals. Little design information is given for desired filter specifications (e.g. passband ripple, rejection level, and equal-ripple stopband starting frequency for elliptic-function low-pass filters). On the other hand, the low-pass filters using slotted ground structure [28], [29] have been recently reported. However, as mentioned in [29], the filter [28] using open stubs and high-impedance line occupies a large circuit size. With a wide microstrip line, the filter in [29] eliminates the need for the open stubs and high-impedance lines, but only Chebyshev low-pass filters have been reported, and no elliptic-function low-pass filters have been studied.

In this chapter, design methods for microstrip elliptic-function low-pass filters using distributed elements or slotted ground structure are presented. The transmission-line model and full-wave simulation are used to calculate the equivalent *L*-*C* values of the microstrip line sections, the interdigital capacitor, and the slotted ground structure. Because no lumped component is used, it is easy to fabricate these planar filters. For the filters using an interdigital capacitor, because the interdigital capacitor can provide a bigger parallel capacitance, the finite attenuation pole can be located closer to the passband, thus achieving a sharper cutoff frequency response. The filter using a slotted ground structure has the advantage of easy synthesis for the desired *L*-*C* values. The design concepts of these two filters are all validated through simulations and measurements with good agreement as discussed in Sections 2 and 3. The comparison between these filters is outlined in Section 4.

4.2 Elliptic-function lowpass filters using distributed elements

For low frequency filters, discrete lumped elements are used to realize the required *L*-*C* values. However, for high frequency filters, not only the soldering but also the size of the lumped elements that are no longer small in comparison with the wavelength can cause parasitic problems. To eliminate the soldering problems, distributed elements are used in microwave/millimeter-wave bands. By using a simple transmission-line model and full-wave simulation, the equivalent *L*-*C* values of the distributed elements are calculated within the passbands. Although the desired passband response can be predicted very well, the stopband response is different from that of the discrete ideal lumped element filter. Therefore, full-wave simulations should be carried out to predict the stopband response. Nevertheless, the required *L*-*C* values and the calculated *L*-*C* values of the distributed elements still provide useful design information and help the full-wave optimization.

Fig. 25(a) shows the configuration of the elliptic-function low-pass filter. The filter consists of a microstrip line section in parallel with an interdigital capacitor. Fig. 25(b) shows the equivalent circuit, where L_s is the equivalent inductance of the microstrip line section, C_g is the equivalent series capacitance of the interdigital capacitor, and C_{ps} is the sum of the equivalent shunt capacitances of the microstrip line section and the interdigital capacitor. The transmission-line model is used to calculate the equivalent circuit elements of the microstrip line section. Since the structure of the interdigital capacitor is complicated, parasitic effects should also be considered using full-wave simulator together with transmission-line model calculation.

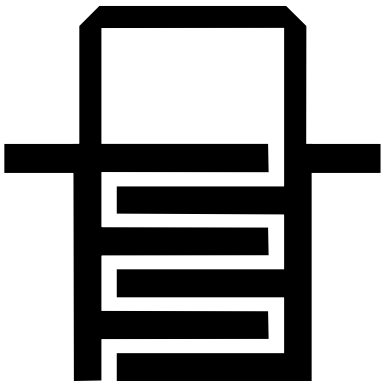

(a)

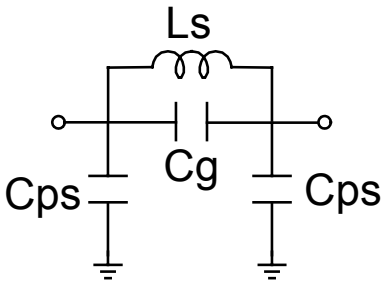

(b)

Fig. 25. Microstrip elliptic-function low-pass filter using distributed elements (a) schematic and (b) equivalent circuit model.

Fig. 26(a) shows the schematic and the equivalent π-network circuit of the microstrip line section. For a lossless single transmission line with the electrical length of θ, the equivalent inductance L_s, and capacitance C_s are given by [26]

$$L_s = \frac{Z_s \sin\theta}{\omega} \quad \text{(H)} \tag{4a}$$

$$C_s = \frac{1-\cos\theta}{\omega Z_s \sin\theta} \quad \text{(F)} \tag{4b}$$

where Z_s is the characteristic impedance of the transmission line section, and ω is the

angular cutoff frequency.

Fig. 26(b) shows the schematic and the equivalent π-network circuit of the interdigital capacitor. In order to take all discontinuities into consideration, assuming a lossless and symmetrical case, a full-wave electromagnetic simulator* is used to calculate the two-port *Y*-parameters of the specific interdigital capacitor, and then the equivalent capacitances C_g and C_p are given by [19], [30]

$$C_g = -\frac{\mathrm{Im}(Y_{21})}{\omega} \tag{5a}$$

$$C_p = \frac{\mathrm{Im}(Y_{11} + Y_{21})}{\omega} \tag{5b}$$

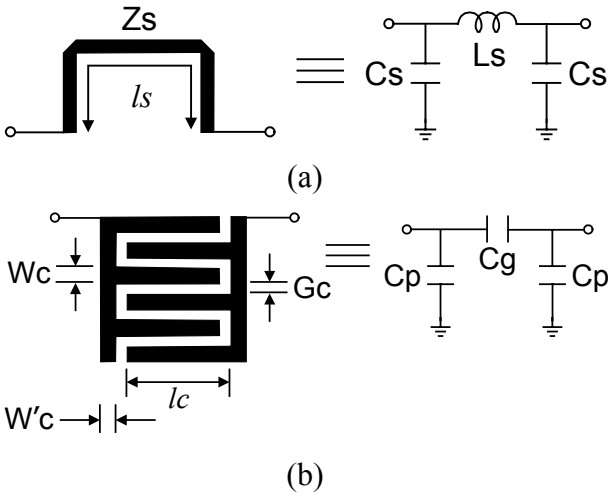

Fig. 26. Schematic and equivalent circuit model of the (a) microstrip line section and (b) interdigital capacitor.

To gain an insight of the relation between the interdigital capacitor dimensions and

* IE3D version 10.2, Zeland Software Inc., Fremont, CA, 2004.

capacitance values, many full-wave simulations of different interdigital capacitors were carried out to synthesize the required capacitances. Fig. 27 shows a design figure of C_g and C_p versus finger numbers. The substrate is a 25 mil RT/Duroid 6010.8 substrate with a dielectric constant of 10.8. The dimensions are: $W_c = W'_c = 0.3$ mm, $l_c = 2$ mm, $G_c =$ 0.2 or 0.4 mm, and finger number = 2, 4, 6, and 8. It shows that C_g and C_p increase as finger numbers increases, C_g deceases as G_c increases, while C_p increases as G_c increases due to more metal coverage. Since there are many parameters (W_c, l_c, and G_c) that can be varied, it is easier to realize the required capacitors C_g and C_p in this filter than in a filter using couple-lines [26].

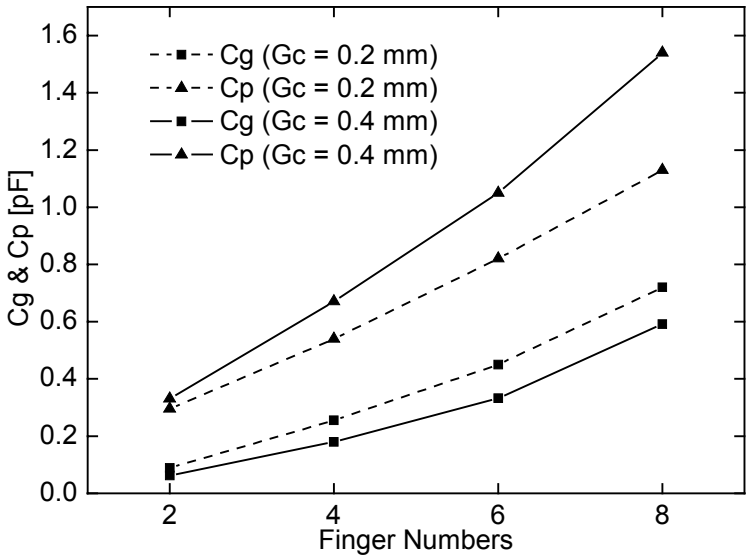

Fig. 27. C_g and C_p values with different finger numbers. Dash line: $G_c = 0.2$ mm, solid line: $G_c = 0.4$ mm.

The prototype elliptic-function low-pass filter element values [19] for n = 3,

passband ripple L_{Ar} = 0.1 dB, and stopband attenuation L_{As} = 18.86 dB with the equal-ripple stopband starting normalized frequency $\Omega_s = 1.6949$ are: g_1 = 0.8333, g_2 = 0.84, g'_2 = 0.33, and g_3 = 0.83. The required *L*-*C* values are calculated by [19]:

$$L_{s,\mathrm{Required}} = \frac{Z_0 g_2}{2\pi f_c} = 3.37 \text{ nH} \tag{6a}$$

$$C_{g,\mathrm{Required}} = \frac{g'_2}{Z_0 \times 2\pi f_c} = 0.52 \text{ pF} \tag{6b}$$

$$C_{ps,\mathrm{Required}} = \frac{g_1}{Z_0 \times 2\pi f_c} = 1.33 \text{ pF} \tag{6c}$$

where the cutoff frequency is f_c = 2 GHz, and Z_0 is the source/load impedance of 50 ohm. In order to realize the circuit element L_s = 3.37 nH, one can use Eq. (4) to calculate Z_s and θ as 72 ohm and 36°, respectively, and consequently L_s = 3.37 nH, and C_s = 0.36 pF. From Fig. 27, when the finger number = 6 and G_c = 0.2 mm, it shows that C_g = 0.45 pF, C_p = 0.82 pF, and then $C_{ps} = C_p \,//\, C_s = C_p + C_s$ = 1.18 pF, which is close to the required *L*-*C* values.

Fig. 28 shows the schematic of the low-pass filter with W_s = 0.23 mm, l_s = 5.06 mm, $W_c = W'_c$ = 0.3 mm, G_c = 0.2 mm, and l_c = 2 mm. Fig. 29 shows the simulated and measured results. The full-wave simulation is obtained by IE3D[1], and the results for the required and the approximately calculated *L*-*C* values are obtained by using AWR Microwave Office[2]. From dc to 2 GHz, the return loss is better than 16 dB and the

[1] IE3D version 10.2, Zeland Software Inc., Fremont, CA, 2004. [2] Microwave Office 2005, Applied Wave Research Inc., El Segundo, CA, 2005.

insertion loss is less than 0.51 dB. An attenuation pole is located at 3.1 GHz. For the stopband response, the full-wave simulation agrees better with the measured results, when compared to the simulated results of the required *L*-*C* values and the approximately calculated *L*-*C* values. This is because the equivalent *L*-*C* values of the distributed elements are calculated according to the passband characteristics only.

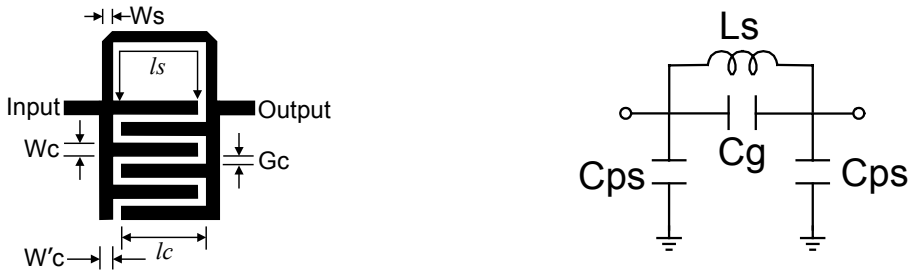

Fig. 28. Elliptic-function low-pass filter using distributed elements. (a) schematic and (b) equivalent circuit model. ($C_{ps} = C_p + C_s$).

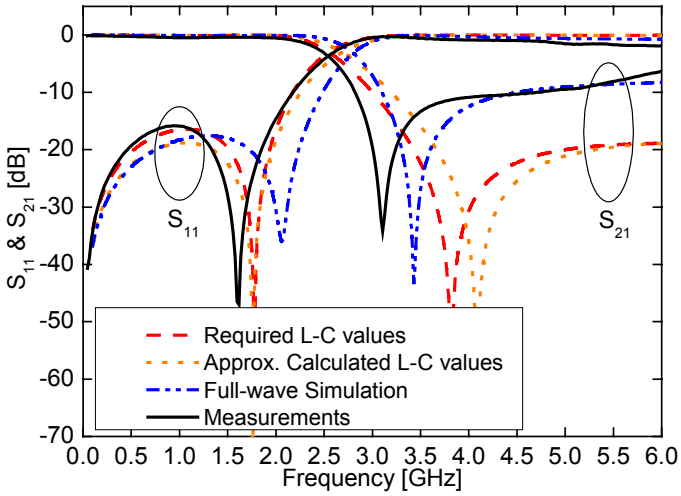

Fig. 29. Simulated and measured results of the low-pass filter using distributed elements.

4.3 Elliptic-function lowpass filter using slotted ground structure

Fig. 30 shows the 3-pole elliptic-function low-pass filter using a slotted ground structure. The filter consists of a low-impedance microstrip line and a dumbbell slotted ground structure located under the center of the line. The equivalent circuit model for the slotted ground structure is a parallel L_{SGS}-C_{SGS} tank [28], [29], where L_{SGS} and C_{SGS} are determined by the two square apertures and the thin slot, respectively. The equivalent circuit model for the low-impedance line consists of two shunt capacitors (C_M).

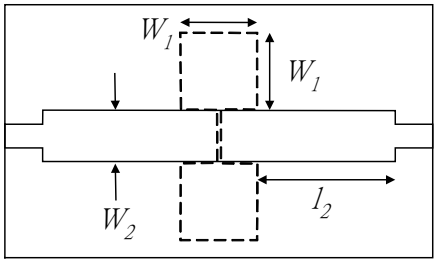

(a)

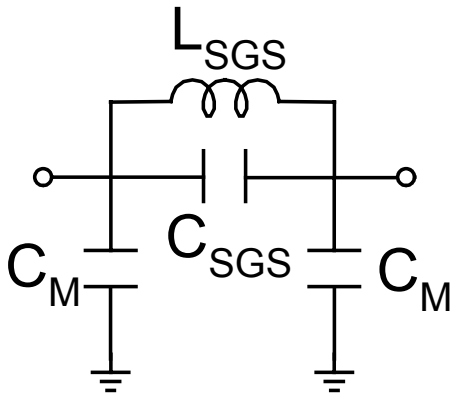

(b)

Fig. 30. Elliptic-function low-pass filter using slotted ground structure. (a) schematic (dashed line shows a dumbbell slotted ground structure) and (b) equivalent circuit model.

To obtain the equivalent L_{SGS}-C_{SGS} values of the slotted ground structure, full-wave

simulated results are first obtained by using IE3D[1]. Fig. 31 shows the simulated results of the full-wave simulation and the circuit simulation. The circuit simulation is obtained by using AWR Microwave Office[2]. The parameters of the slotted ground structure are: W_1 = 5 mm, W_2 = 3.5 mm, width of thin slot = 0.2 mm, and length of thin slot = 3.5 mm. The substrate is a 20-mil RT/Duroid 5880 substrate with a dielectric constant of 2.2.

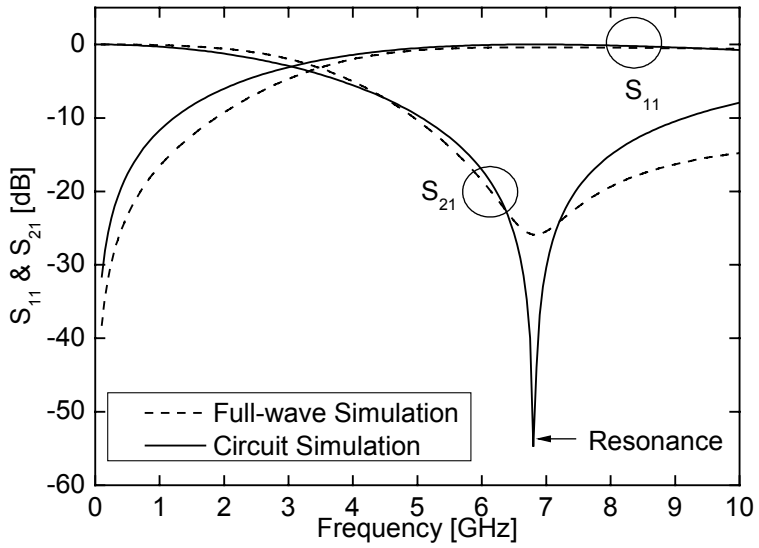

Fig. 31. Simulated results of a slotted ground structure. (W_1 = 5 mm, W_2 = 3.5 mm, width of thin slot = 0.2 mm, and length of thin slot = 3.5 mm).

Given the required *L*-*C* values, one can calculate the equivalent L_{SGS} and C_{SGS} by using [29]:

$$X_{L_{\mathrm{Required}}C_{\mathrm{Required}}} = \frac{L_{\mathrm{Required}} / C_{\mathrm{Required}}}{\left(\omega_c C_{\mathrm{Required}}\right)^{-1} - \omega_c L_{\mathrm{Required}}} \tag{7a}$$

[1] IE3D version 10.2, Zeland Software Inc., Fremont, CA, 2004. [2] Microwave Office 2005, Applied Wave Research Inc., El Segundo, CA, 2005.

$$C_{SGS} = \left(\omega_0 X_{L_{\mathrm{Re}\,quired} C_{\mathrm{Re}\,qureid}} \left(\frac{\omega_0}{\omega_c} - \frac{\omega_c}{\omega_0} \right) \right)^{-1} \tag{7b}$$

$$L_{SGS} = \left(C_{SGS} \omega_0^2 \right)^{-1} \tag{7c}$$

where ω_c is the angular cutoff frequency of the low-pass filter and ω_0 is the resonant angular frequency of the slotted ground structure. When the cutoff frequency = 2 GHz, and the resonant frequency = 6.8 GHz by observing Fig. 31, C_{SGS} = 0.13 pF and L_{SGS} = 4.2 nH. As shown in Fig. 31, the circuit's simulated results using the above circuit element values show a good agreement with the full-wave simulated results.

The slotted ground structure is then used to build an elliptic-function low-pass filter. From the elliptic-function low-pass prototype filter tables, the element values for n = 3, passband ripple L_{Ar} = 0.1 dB, and stopband attenuation L_{As} = 35 dB with the equal-ripple stopband starting normalized frequency $\Omega_s = 2.921$ are: g_1 = 0.958, g_2 = 1.057, g'_2 = 0.0837, and g_3 = 0.958. Similar to (6), for the cutoff frequency f_c = 2 GHz, the required *L*-*C* values can be calculated with:

$$L_{\mathrm{Re}\,quired} = \frac{Z_0 g_2}{2\pi f_c} = 4.2 \text{ nH} \tag{8a}$$

$$C_{\mathrm{Re}\,quired} = \frac{g'_2}{Z_0 \times 2\pi f_c} = 0.13 \text{ pF} \tag{8b}$$

$$C_{M,\mathrm{Re}\,quired} = \frac{g_1}{Z_0 \times 2\pi f_c} = 1.52 \text{ pF} \tag{8c}$$

Therefore, the slotted ground structure with W_1 = 5 mm, W_2 = 3.5 mm, width of thin slot = 0.2 mm, and length of thin slot = 3.5 mm on a 20-mil RT/Duroid 5880

substrate could be readily used. The length of the low-impedance line of W_2 = 3.5 mm for C_M can be found from [19]:

$$l_2 = \frac{\lambda_g}{2\pi}\sin^{-1}(\omega_c C_M Z_0) \tag{9}$$

where Z_0 is 27.7 ohm for the low-impedance microstrip line and λ_g =106.5 mm at the cutoff frequency of 2 GHz. Hence, l_2 = 9.5 mm.

Fig. 32 shows the simulated and measured results for the elliptic-function low-pass filter. The full-wave simulation is obtained by IE3D[1], and the required *L*-*C* values simulation is obtained by AWR Microwave Office[2]. The measured results show a good agreement with the full-wave simulated results. From dc to 1.8 GHz, the return loss is better than 15 dB and the insertion loss is less than 0.5 dB.

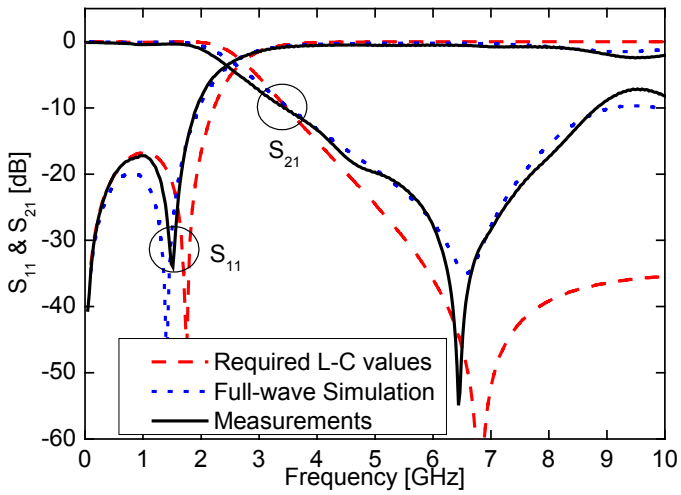

Fig. 32. Simulated and measured results of low-pass filter using slotted ground structure.

[1] IE3D version 10.2, Zeland Software Inc., Fremont, CA, 2004. [2] Microwave Office 2005, Applied Wave Research Inc., El Segundo, CA, 2005.

4.4 Discussions and comparisons

The above two filters are discussed and compared in this section. The filter using distributed elements discussed in Section 2 is referred as filter #1, and the filter using slotted ground structure described in Section 3 is referred as filter #2 for simplicity.

A. Fabrication

Since filter #2 uses slotted ground structure, double-side etching is required. Therefore, an accurate alignment is required and repeatability might be difficult to maintain. On the other hand, filter #1 only requires one-side etching and is easier to fabricate.

B. Design method

For filter #1, $C_{ps} = C_s + C_p$. Since C_s and C_p are dependent on the selecting of L_s and C_g, respectively, there is less freedom in choosing C_{ps} after L_s and C_g are determined. Therefore, approximation and a time-consuming iteration process are needed. On the other hand, for filter #2, C_M is independent of L_{SGS} and C_{SGS}. The design procedure is direct and easier.

C. Integration

Since filter #2 uses a slotted ground structure, tackling the radiation loss problem [29] and the requirement of a special fixture to prevent shorting the slotted ground structure could make it inconvenient to integrate with other components.

To further compare these two filters, filter #1 is fabricated on the same 20-mil RT/Duroid 5880 substrate and with the same specifications of filter #2 in Section 3 (n =

3, passband ripple L_{Ar} = 0.1 dB, and stopband attenuation L_{As} = 35 dB with the equal-ripple stopband starting normalized frequency $\Omega_s = 2.921$). By using the design procedure in Section 2, Fig. 33 shows the design schematic and parameters of filter #1. In this case, it should be noted that the sum of C_s and C_p is less than the required C_{ps}, and two low-impedance lines (W_3, l_3) are used to introduce a bigger shunt capacitance.

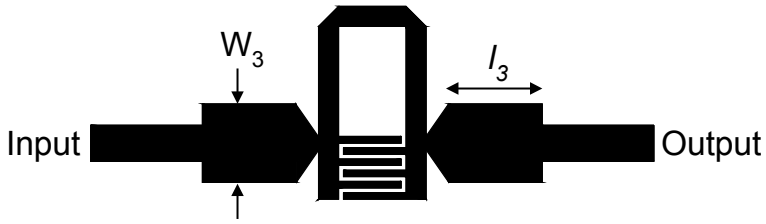

Fig. 33. Schematic of the low-pass filter for comparison. W_3 = 3.5 mm, l_3 = 4.2 mm, (refer to Fig. 26(a)) l_s = 12.8 mm, W_s = 0.9 mm, W_c = 0.3 mm, G_c = 0.2 mm, l_c = 2.8 mm, and W'_c = 0.9 mm.

Fig. 34 shows the measured results of these two filters with the following observations.

D. Insertion loss

As shown in Fig. 34(b), filter #2 has a smaller insertion loss than filter #1 by 0.1 dB (average).

E. Circuit size

The circuit size of filter #1 is 15.2 x 8.6 mm^2, and the circuit size of filter #2 is 24 x 13.5 mm^2. Filter #1 shows a 60 % size reduction in comparison with filter #2.

F. Stopband rejection

Filter #2 shows a better stopband rejection than filter #1. Filter #2 shows not only a better rejection level but also a wider stopband bandwidth.

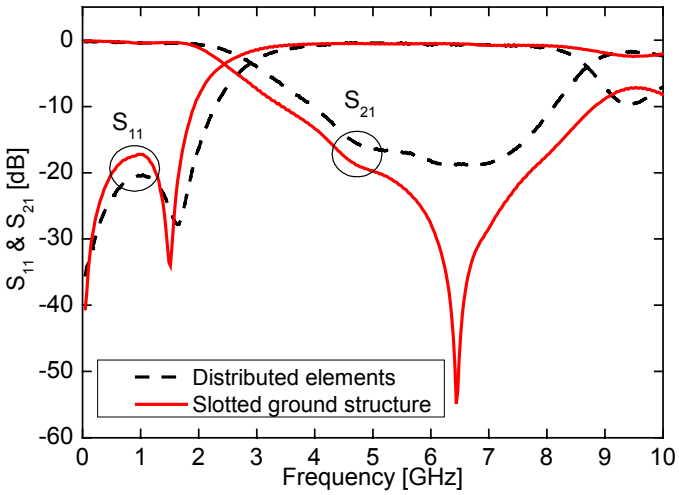

(a)

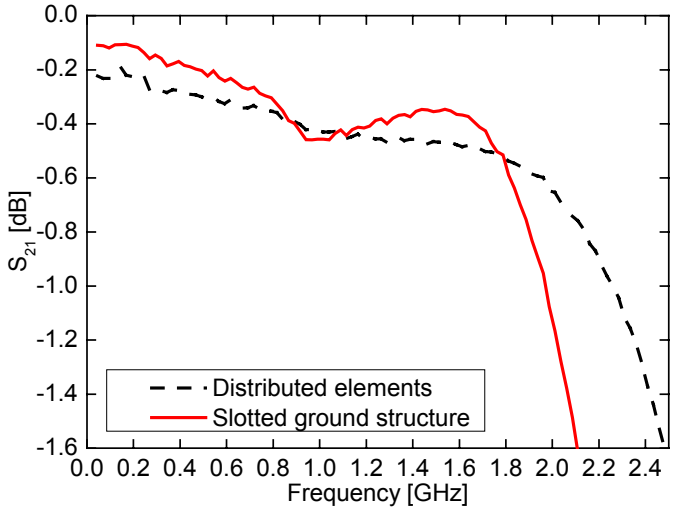

(b)

Fig. 34. Measured results of low-pass filters using distributed elements (filter #1) or slotted ground structure (filter #2). (a) whole frequency range and (b) enlarged view within passband.

4.5 Conclusions

The design of the microstrip elliptic-function low-pass filters using distributed elements or slotted ground structure has been investigated. With the aid of transmission-line model calculation and full-wave simulation, the equivalent *L*-*C* values for the low-pass filters have been derived. The measured results show good agreement with the full-wave simulated results. Discussions and comparison of these two filters are also given. These filters should find many applications in microwave/millimeter-wave systems.

CHAPTER V

BANDPASS FILTERS WITH HARMONIC SUPPRESSION*

5.1 Introduction

In this chapter, three conventional bandpass filters with suppression of spurious passbands are studied. The harmonic suppression is achieved by modifying the configurations of the filters instead of cascading additional bandstop filters or lowpass filters which increases the circuit sizes and the insertion loss in the passband.

Dual-mode resonators have been widely used in microwave bandpass filters. One of the most important advantages of the dual-mode resonators is that each resonator can be used as a doubly tuned resonant circuit. Consequently, the number of resonators for a n-degree filter can be reduced by half, and then the size of the filter can be compact [19]. Dual-mode square patch resonator has been used to build Chebyshev and Elliptic filters [31]. However, the conventional square patches suffer from their large size. To reduce the circuit size, the patches with the tilt crossed slots [32], [33] or circular slots [34] have been proposed. Although these filters miniaturize the circuit size, the inherently second harmonic passband problem is still not solved.

---

* Parts of this chapter are reprinted, with permission, © 2005 IEEE from W.-H. Tu and K. Chang, "Miniaturized Dual-mode Bandpass Filter with Harmonic Control," *IEEE Microw. Wireless Compon. Lett.*, vol. 15, no. 12, pp. 838-840, Dec. 2005., © 2006 IEEE W.-H. Tu and K. Chang, "Compact second harmonic-suppressed bandstop and bandpass filters using open stubs," *IEEE Trans. Microw. Theory Tech*., vol. 54, no. 6, pp. 2497–2502, June 2006., and © 2006 IEEE W.-H. Tu, H. Li, K. A. Michalski, and K. Chang, "Microstrip Open-Loop Ring Bandpass Filter using Open Stubs for Harmonic Suppressio*n*," in 2006 *IEEE MTT-S Int. Microw. Symp*., Jun. pp. 357-360.

In section 2, a miniaturized dual-mode resonator/filter with right crossed slots is introduced. Similar to the tilt structure, the right crossed slots perturb the fundamental resonance and lower the resonant frequency, which makes the square patch resonator compact. On the other hand, the right crossed slots only slightly perturb the second resonance and keep the second resonant frequency unchanged, which makes the fundamental and second resonance frequencies further apart. The single-mode and dual-mode square patch resonators with right crossed slots are analyzed via the full-wave simulation. The bandpass filter using the proposed dual-mode resonator shows a 4.4 % fractional bandwidth at 1.595 GHz with a return loss of better than 10 dB and insertion loss of less than 2.5 dB, while the second passband is located around 4.6 GHz.

Bandpass filters are essential components in modern communication systems. Several literatures of distributed filters such as end-coupled filter [35], parallel-coupled filter [36], and cross-coupled filter [30] have been reported. Given the filter specifications together with the well-documented design methods, these filters could be designed for the fundamental frequency band. However, due to the distributed characteristics of the transmission lines, these filters suffer from the spurious passbands. Many useful methods [37]-[44] have shown promising results dealing with the harmonic problems. Filters using stepped-impedance resonator move the second passband higher to more than two times the fundamental frequency [37]. Furthermore, controlling the input and output tapping could have extra transmission zeros in the stopband [38]. Etched Bandgap-based filter has shown over 25-dB rejection at the second harmonic [39]. The shunt quarter-wavelength open stubs were introduced to create transmission

zeros at the stopband [40], [41]. The corrugated [42] and wiggly [43], [44] line filters have second harmonic suppression improvement over 30 dB.

In section 3, the concept in [44] is adopted and further studied for the open-loop filter [23]. By adding a short open stub in the center of the half-wavelength resonator, the fundamental resonant frequency remains unchanged, and the second harmonic resonance is perturbed by the stub and no longer appears at two times the fundamental frequency. In [44], the relation between the electrical length of the short open stub and the second resonant frequency is not outlined. With the ABCD matrix calculation, the relation between the electrical length of the shunt open stub and the second resonant frequency is derived. The design concept of the proposed filter is validated through simulation and experiments showing better suppression performance over conventional filters.

In section 4, the concept of integrating bandstop filters into the conventional open stub bandpass filter is described. By replacing the series connecting lines of a conventional open-stub bandpass filter with the equivalent T-shaped lines, the proposed filter have a compact size and an improved second harmonic suppression. Similar method has been reported [45], [46]. However, there is no design equation for the equivalent lines and the design is dependent on time-consuming iterative procedure [45]. In [46], although the design equations are given, the equations are only for a special case (all lines are of same characteristic impedance). In [40], a quarter-wavelength shunt open stub is added to a fixed half-wavelength resonator to introduce an attenuation pole and work as a K-inverter. For the proposed filter, on the other hand, general design equations

for generating the parameters of the equivalent T-shaped lines are derived by using transmission-line model calculation. The equivalent T-shaped lines show good similarities with the original line around the specific fundamental passband. Hence, the passband response of the proposed filter is the same as the conventional one's. Furthermore, the T-shaped line works like a bandstop filter at the second harmonic. Therefore, the proposed filter has better second harmonic rejection than conventional one. The concept of the proposed filter is validated by simulations and experiments. The proposed filter has improved second harmonic suppression with a compact size.

5.2 Miniaturized dual-mode bandpass filter with harmonic control

A. Single-mode resonators

Fig. 35 shows the configurations of the three dual-mode resonators. The conventional one as shown in Fig. 35(a) is consisted of a square patch with an isosceles triangle cut. The lateral side ΔL of the triangle controls the coupling between the two orthogonal modes. As shown in Fig. 35(b), a dual-mode resonator with the tilt [32], [33] is introduced for miniaturization. The crossed slots can perturb and reroute the current distribution. The current path is lengthened, and the resonant frequency is lowered.

To see how the crossed slots influence the resonant frequencies of the dual-mode patch, single-mode resonators (i.e. no perturbation at symmetric plane) of different slot lengths with gap coupling structures are studied. The substrates are 25 mil RT/Duroid 6010.8 with dielectric constant ε_r = 10.8. The dimensions are: L = 20 mm $\approx$ 0.5 λ_g, W = 0.5 mm, and 0.2 mm gap between feed line and resonator, where λ_g is the guided

wavelength at fundamental frequency without the right crossed slots.

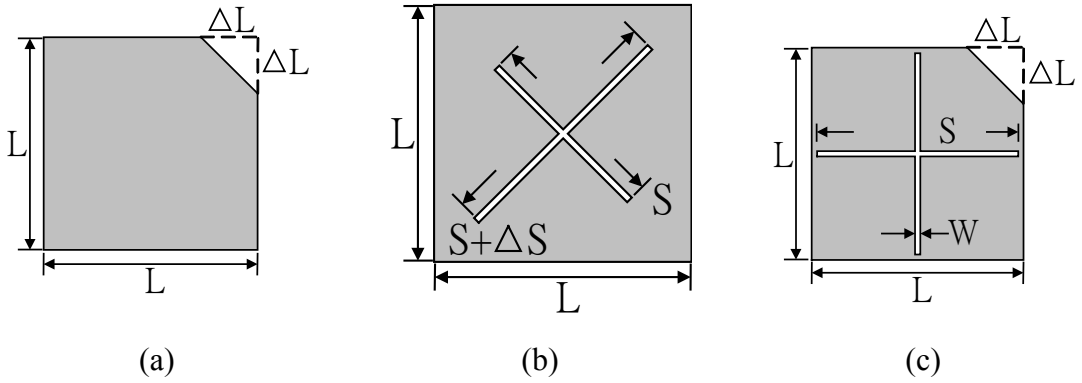

Fig. 35. Configurations of dual-mode resonators (a) conventional (b) tilt crossed slot [32], [33] and (c) proposed.

For the right crossed slots case, Fig. 36 shows the simulated insertion loss of different slot lengths *S*. The simulation is carried out using IE3D software*. When $S = 0$ mm, the single-mode patch becomes a conventional single- mode resonator with the fundamental frequency at 2.3 GHz and the second harmonic at 4.6 GHz. When the slot length *S* increases, the fundamental frequency drops and the second harmonic frequency is unchanged. This makes the resonator effectively have second resonant frequency much higher than twice the fundamental resonant frequency. The reason for this phenomenon can be explained by the current distribution of the fundamental and second resonance as shown in Fig. 37. For the fundamental resonance, the horizontal slot has a little effect on the current flow since it is parallel to the current distribution. On the other hand, the vertical slot has a strong effect in changing the current distribution and thus

* IE3D version 10.2, Zeland Software Inc., Fremont, CA, 2004.

makes the fundamental frequency drop. For the second resonance, both the horizontal and vertical slots are parallel to the current distribution; therefore they have little effect on the current distribution resulting in little change in the resonant frequency. Furthermore, the simulated unloaded Q of the proposed resonator (S = 16 mm) is 282.63 and the simulated unloaded Q of the conventional single-mode resonator of the same resonant frequency is 225.24. This implies that the total loss (dielectric loss, conductor loss, and radiation loss) of the proposed resonator is less than that of the conventional resonator.

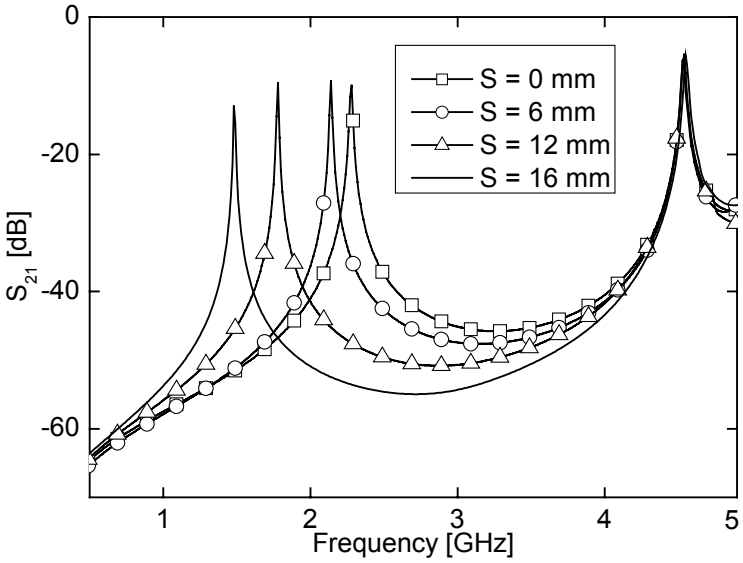

Fig. 36. Simulated results of the single-mode right crossed slot resonator. W = 0.5 mm.

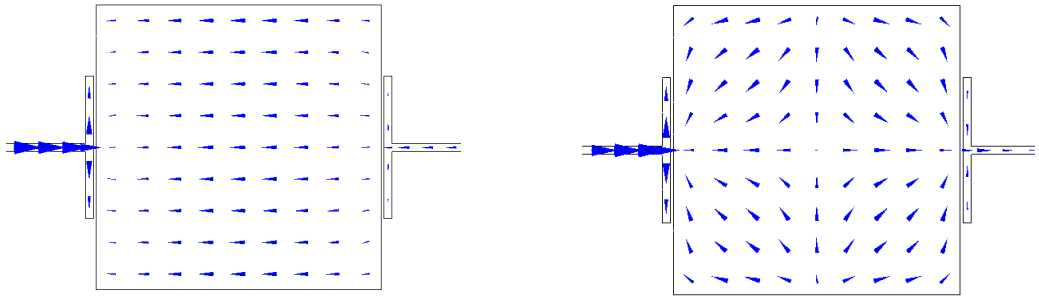

(a) (b)

Fig. 37. Current distributions of (a) the fundamental (2.3 GHz) mode and (b) the second (4.6 GHz) mode. S = 0 mm.

B. Dual-mode bandpass filter

Fig. 38(a) shows the configuration of the proposed miniaturized dual-mode bandpass filter with right crossed slots. The two 50 ohm feed lines of width = 0.57 mm are connected directly to the patch in order to reduce the insertion loss caused by the gap coupling structure. From 1.56 to 1.63 GHz (4.4 % fractional bandwidth), the measured return loss is better than 10 dB and insertion loss is less than 2.5 dB. The second passband is located around 4.6 GHz = 2.88f_o, where f_o = 1.595 GHz.

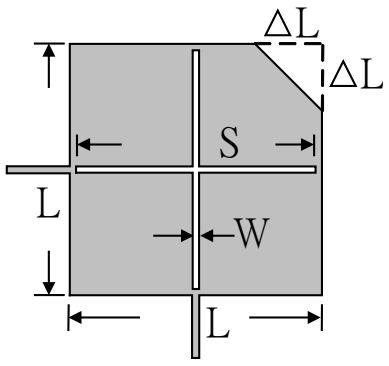

(a)

Fig. 38. The proposed dual-mode bandpass filter. (a) configuration (b) whole frequency range and (c) near passband. W = 0.5 mm, L = 20 mm, ΔL= 5.1 mm, and S = 16 mm.

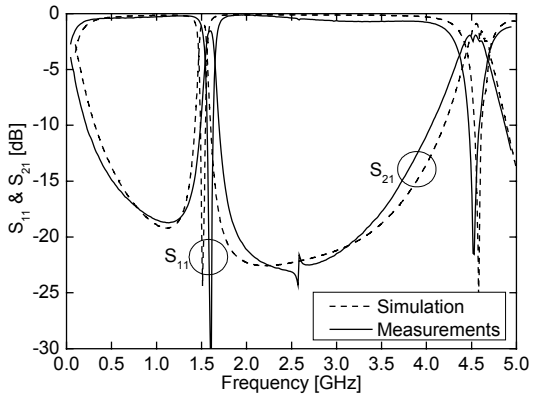

(b)

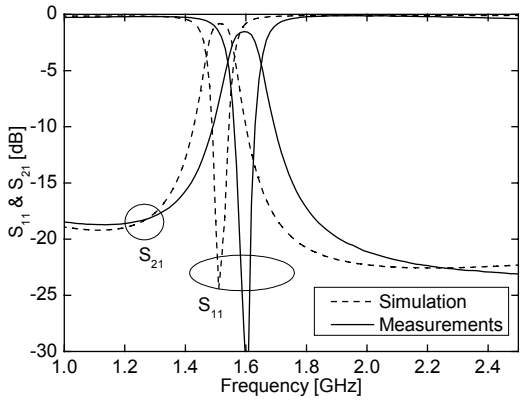

(c)

Fig. 38. Continued.

5.3 Microstrip open-loop ring bandpass filter using open stubs for harmonic suppression

A. Half-wavelength resonators with shunt open stubs

Fig. 39(a) shows the conventional half-wavelength resonator (Z_1, L_1) with end-coupling scheme, and Fig. 39(b) shows the half-wavelength resonator with a shunt open stub (Z_2, L_2) at its center, where L_2 is smaller than quarter guided wavelength. For

the conventional resonator, it shows resonances at the frequencies of nf_0, where f_0 is the fundamental frequency and n = 1, 2, 3…. For the resonator with a shunt stub, its fundamental frequency is the same as the conventional one's. On the other hand, its second resonance frequency is smaller than $2f_0$. At fundamental frequency, the two open ends of the half-wavelength resonator transform into a virtually short circuit at the center of the resonator, and the shunt open stub has the smallest effect on the resonant frequency. At the second harmonic frequency $2f_0$ of the conventional resonator, the two open ends of the half-wavelength resonator transform into a virtually open circuit at the center of the resonator, and the shunt open stub perturbs the resonant frequency. In fact, because the current distribution is lengthened, the second resonant frequency of the resonator with stub drops and is smaller than $2f_0$.

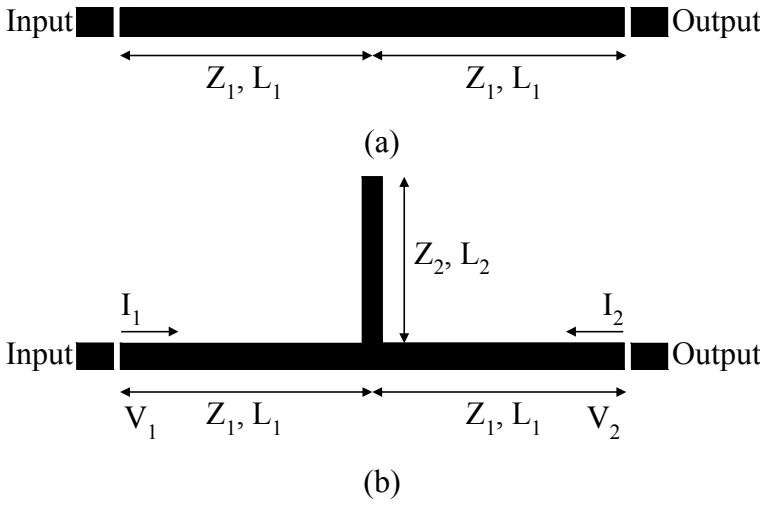

Fig. 39. Schematics of the (a) conventional half-wavelength resonator and (b) half-wavelength resonator with shunt open stub.

Fig. 40 shows the simulated insertion loss of the conventional resonator ($L_2 = 0$) and the resonator with shunt open stub. The simulation is carried out by IE3D*. The substrate is a 25-mil RT/Duroid 6010.2 substrate with dielectric constant of 10.2. The size of the coupling gap is 0.2 mm. All the line widths for the microstrip are 0.55 mm for 50-ohm lines. L_1 is chosen as 13.93 mm for fundamental resonant frequency of 4 GHz. When L_2 = 0 mm, the resonator with stub (Fig. 39(b)) reduces to the conventional resonator (Fig. 39(a)), and resonance occurs at 4 GHz, 8 GHz, 12 GHz and so on. When L_2 = 3 mm, the resonance occurs 4 GHz and 6.28 GHz, and as expected, no resonance occurs at 8 GHz. When $L_2 = L_1/4$ = 3.5 mm, the resonance occurs at 4 GHz and 5.94 $\cong$ 4 x 1.5 GHz, and again, no resonance occurs at 8 GHz. Furthermore, it should be noted that there is a transmission zero around 8 GHz due to that the shunt stub is quarter-wavelength at 8 GHz [44].

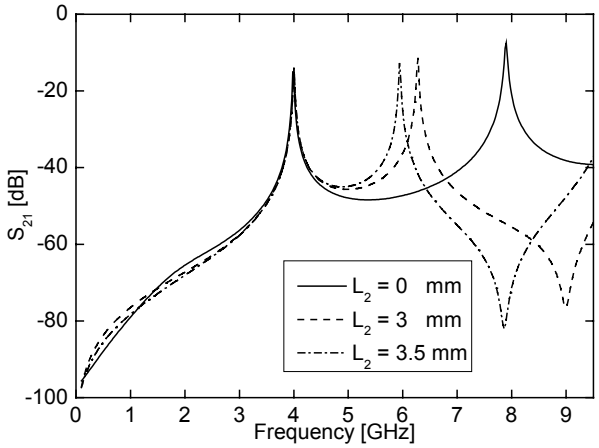

Fig. 40. Simulated insertion loss of resonator in Fig. 37(b).

* IE3D version 10.2, Zeland Software Inc., Fremont, CA, 2004.

Although using the shunt open stub can shift the resonance from $2f_0$ and manipulate the second resonant frequency, there is no design equation to determine the relation between the shunt open stub and the second resonant frequency. Therefore, the ABCD matrix is used for this purpose. Ignoring the effects of discontinuities, the ABCD matrix of the resonator with stub is:

$$M_T = \begin{bmatrix} A_T & B_T \\ C_T & D_T \end{bmatrix} = M_1 M_2 M_1 \tag{10}$$

where

$$M_1 = \begin{bmatrix} \cos R\theta_1 & jZ_1 \sin R\theta_1 \\ jY_1 \sin R\theta_1 & \cos R\theta_1 \end{bmatrix}$$

$$M_2 = \begin{bmatrix} 1 & 0 \\ jY_2 \tan R\theta_2 & 1 \end{bmatrix}$$

and $R \equiv f_1 / f_0$ is the ratio of the second resonant frequency and the fundamental frequency, θ_1 and θ_2 are the electrical lengths, and $Z_1=1/Y_1$ and $Z_2=1/Y_2$ are the characteristic impedances. The equation for input/output current of the modified resonator shown in Fig. 39(b) is:

$$I_1 = C_T V_2 - D_T I_2 \tag{11}$$

Since the boundary condition at both ends of the resonator is open circuit, $I_1 = I_2 = 0$ A. Therefore, $C_T = 0$. Assuming $Z_1 = Z_2$ for simplicity, θ_2 can be solved in terms of frequency ratio R and θ_1:

$$\theta_2 = \frac{\tan^{-1}\left(-2\tan(R\theta_1)\right)}{R} \tag{12}$$

Fig. 41 shows the design curve for θ_2, when θ_1 = 90°. When R = 2 (second resonant frequency $f_1 = 2\,f_0$), $\theta_2 = 0^o$ and this is the case in Fig. 40 for L_2 = 0 mm. On the other hand, when R = 1.5 (second resonant frequency $f_1 = 1.5\,f_0$), $\theta_2 = 42.3^o$ and this is approximately the case in Fig. 38 for L_2 = 3.5 mm.

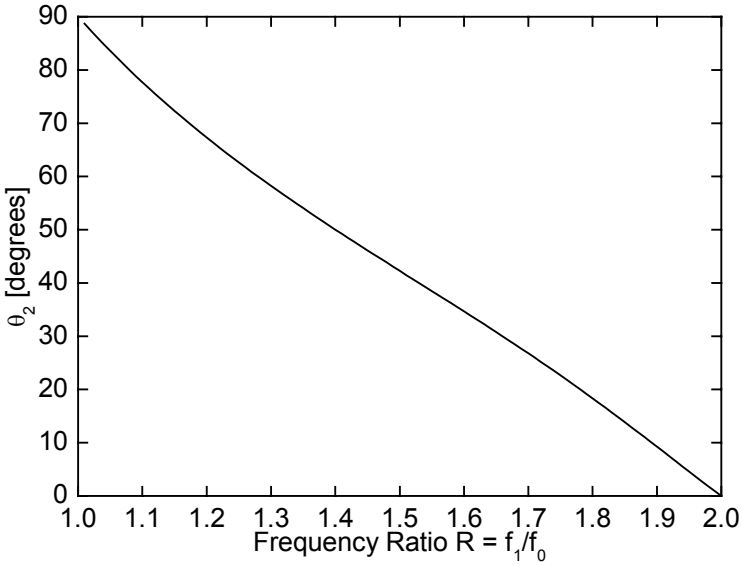

Fig. 41. Design curve for θ_2 with $Z_1 = Z_2$ and $\theta_1 = 90^o$.

B. Open-loop bandpass filter with shunt open stubs

Fig. 42(a) shows the conventional open-loop bandpass filter [5]. The coupling coefficients are: $K_{12} = K_{34}$ = -0.037 and K_{23} = 0.035. The coupling coefficients K_{ij} for resonators i and j can be calculated by [22], [23]:

$$K_{ij} = \pm \frac{f_{p2}^2 - f_{p1}^2}{f_{p2}^2 + f_{p1}^2} \tag{13}$$

where f_{p2} and f_{p1} are the high and low resonant frequencies. The external Q is 15.4 and can be calculated by:

$$Q_{ext} = \frac{f_0}{\Delta f_{\pm 90^o}} \tag{14}$$

where $\Delta f_{\pm 90}{}^{o}$ is the bandwidth of the resonant frequency over which the phase varies from –90° to +90°. Several full-wave simulations have been carried out by IE3D to obtain the resonant frequency, coupling coefficients and external Q. The dimensions of the filter are: L_3 = 11.24 mm, L_4 = 17.61 mm, $G_1 = G_2$ = 0.5 mm, and S_1 = 2.33 mm. All microstrip line widths are 0.55 mm for 50-ohm lines. Fig. 40(b) shows the measured and simulated results. From 1.807 to 1.9015 GHz, the measured return loss is better than 10 dB. The insertion loss is 3 dB at 1.8543 GHz. Furthermore, the second harmonic occurs around 3.7 GHz. The difference between simulated and measured results is mainly due to the fabrication tolerance.

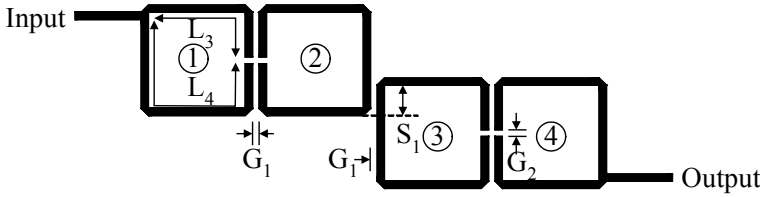

(a)

Fig. 42. (a) Schematics of the conventional open-loop bandpass filter and (b) simulated and measured results.

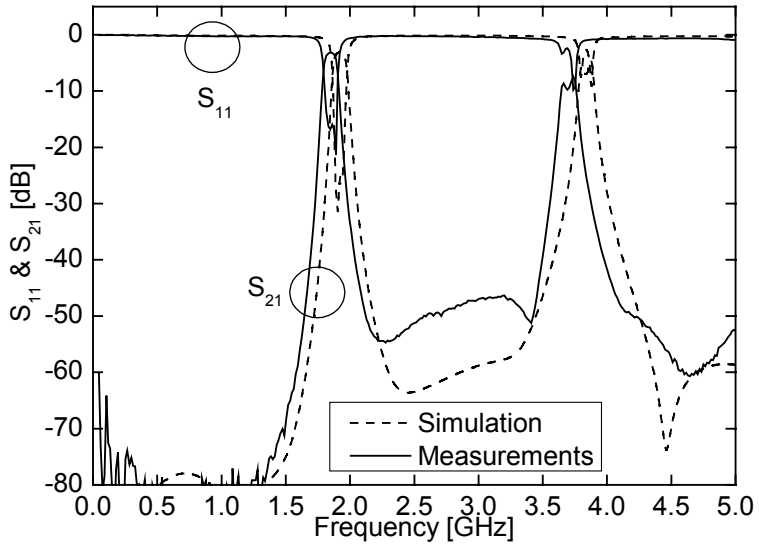

(b)

Fig. 42. Continued.

To suppress the second harmonic, two shunt open stubs are added as shown in Fig. 43(a). When $L_5 = L_6 = 5$ mm, Fig. 43(c) shows the simulated results. Although around 3.7 GHz the filter shows good suppression of 55 dB, the second passband frequency drops to 3.3 GHz with only 11-dB suppression due to that resonator #2 and #3 have their second resonant frequency at 3.3 GHz. To further improve the stopband frequency response, stubs with different lengths ($L_5 = 5$ mm and $L_6 = 7$ mm) are used as shown in Fig 43(b). The resonators #2 and #3 with different stubs have different second resonant frequencies. Resonator #2 with $L_5 = 5$ mm has the second resonant frequency at 3.3 GHz, and resonator #3 with $L_6 = 7$ mm has the second resonant frequency at 2.84 GHz. Since the second resonant frequencies of resonators #2 and #3 are different, the filter has an improved suppression of 35 dB at 3.3 GHz.

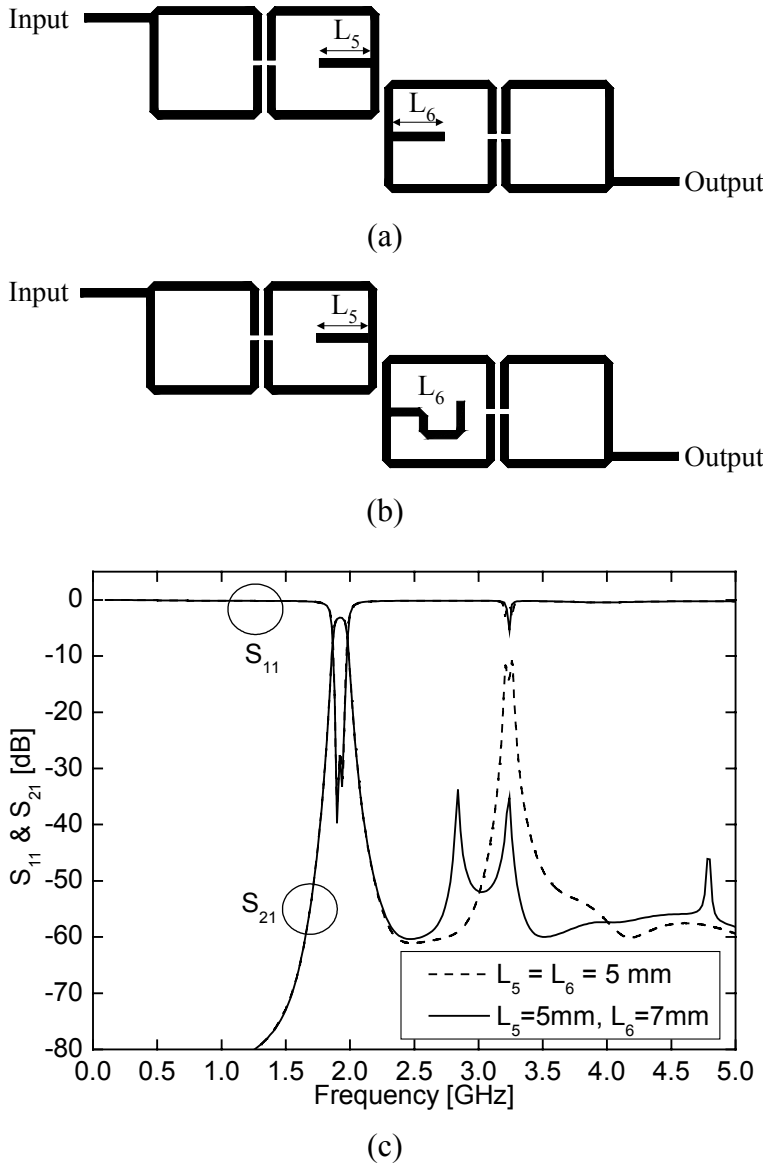

Fig. 43. (a) schematic of filter with identical short open stubs (b) schematic of filter with different short open stubs and (c) simulated results of filters with identical/different stubs.

Fig. 44 shows the simulated and measured results of the filter of different stubs shown in Fig. 43(b). The measured frequency response shifts down slightly due to the fabrication tolerance. From 1.7935 to 1.8835 GHz, the measured return loss is better

than 10 dB. The insertion loss is 3 dB at 1.8385 GHz. Compared with the conventional filter, the spurious passband around 3.7 GHz is suppressed of about 35 dB, and the modified filter shows good stopband response below 1.7 GHz and between 2-6 GHz with suppression of 30 dB. Fig. 45 compares the measured results of the conventional filter and the filter with different stubs. The filter with stubs has improved upper stopband suppression, while the center frequency only shifts down by 0.018 GHz (0.97 %).

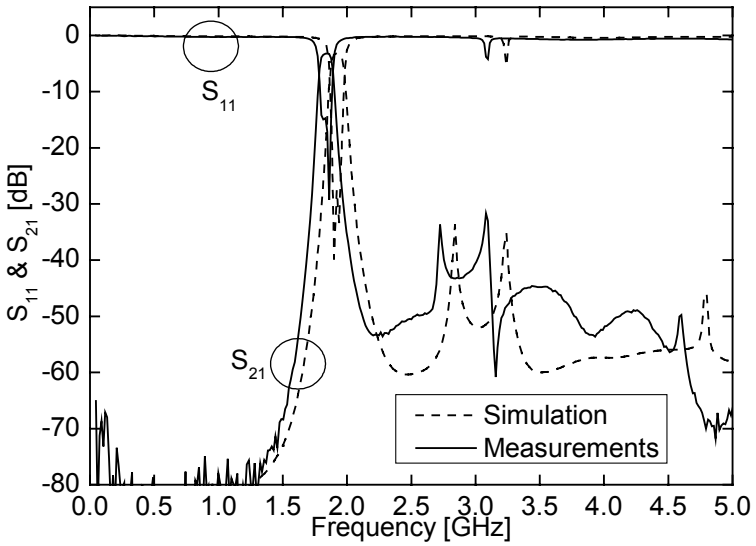

Fig. 44. Simulated and measured results of the bandpass filter with different stubs.

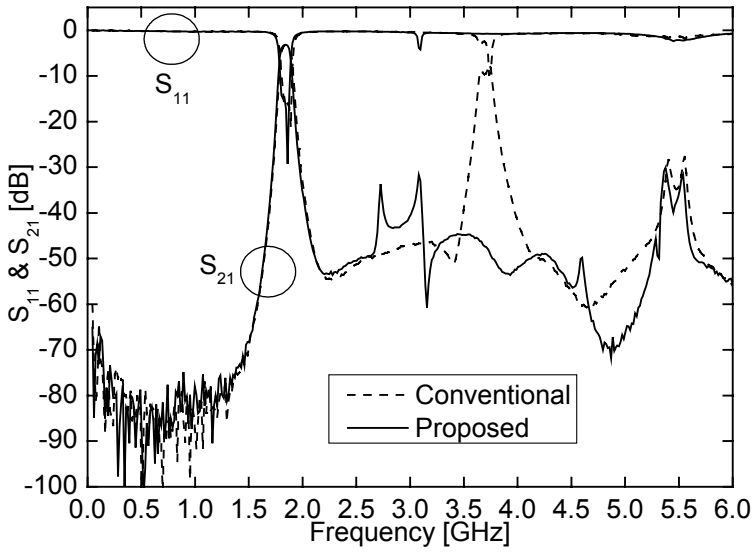

(a)

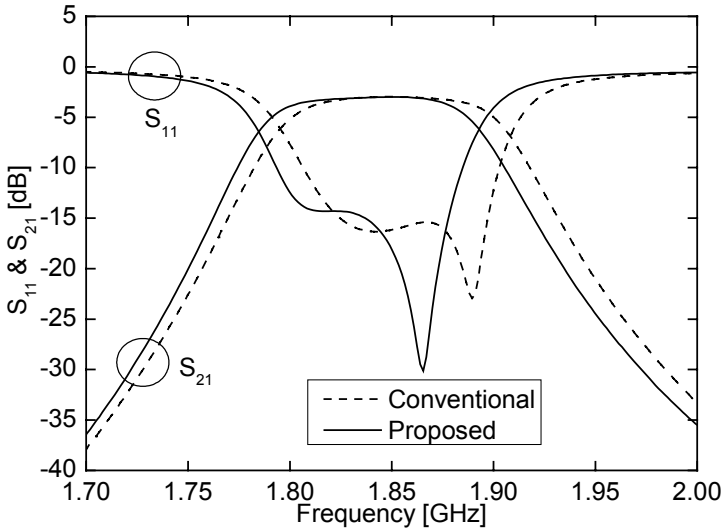

(b)

Fig. 45. Measured results of the conventional and proposed bandpass filters. (a) whole frequency range and (b) near passband response.

5.4 Compact second harmonic-suppressed bandpass filter using open stubs

A. Equivalent T-shaped transmission lines

Fig. 46(a) shows the conventional bandpass filter with open-stub sections separated by quarter-wavelength connecting transmission lines. The connecting transmission line and its equivalent T-shaped transmission line model can be shown in Fig. 46(b) and 46(c), where Z_i is the characteristic impedance and θ_i is the electrical length of the transmission lines (i = 1, 2, 3). The T-shaped transmission line model is consisted of two identical series transmission lines and one shunt open stub located in the center of the two series lines.

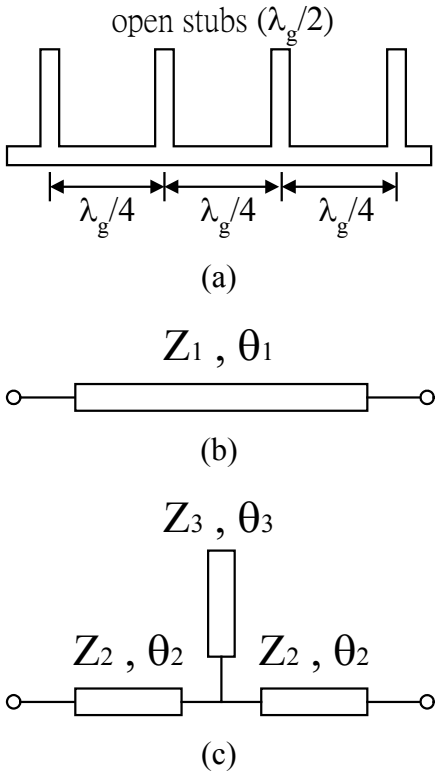

Fig. 46. Schematics of the (a) conventional bandpass filter (b) original connecting transmission line and (c) the equivalent T-shaped transmission line.

To study how the T-shaped transmission line model can be equivalent to the original transmission line, transmission-line model calculation is used. The ABCD matrix of the original transmission line is:

$$M_1 = \begin{bmatrix} \cos\theta_1 & jZ_1 \sin\theta_1 \\ jY_1 \sin\theta_1 & \cos\theta_1 \end{bmatrix} \tag{15}$$

The ABCD matrix of the equivalent T-shaped transmission line model is:

$$M_T = M_2 M_3 M_2 \tag{16}$$

where

$$M_2 = \begin{bmatrix} \cos\theta_2 & jZ_2 \sin\theta_2 \\ jY_2 \sin\theta_2 & \cos\theta_2 \end{bmatrix}$$

$$M_3 = \begin{bmatrix} 1 & 0 \\ jY_3 \tan\theta_3 & 1 \end{bmatrix}$$

Since the T-shaped transmission line is to replace the series quarter-wavelength connecting line, θ_1 is assigned to be 90^o. Therefore, the ABCD matrix of the original transmission line becomes:

$$M_1(\theta_1 = 90^o) = \begin{bmatrix} 0 & jZ_1 \\ jY_1 & 0 \end{bmatrix} \tag{17}$$

On the other hand, since the T-shaped transmission line is designed to have rejection at the second harmonic of the filters, θ_3 is assigned to be 45^o at the fundamental frequency. Therefore, at second harmonic, the electrical length of the shunt stub would be 90^o, and the shunt stub works like a bandstop filter to suppress the second harmonics.

Hence, the ABCD matrix of the shunt stub becomes:

$$M_3(\theta_3 = 45^o) = \begin{bmatrix} 1 & 0 \\ jY_3 & 1 \end{bmatrix} \tag{18}$$

Given that Z_1 would be assigned after completing the conventional filter synthesis, there are three unknown variables remained: θ_2, Z_2, and Z_3. By equating (15) and (16), Z_2 and Z_3 could be solved in terms of θ_2:

$$Z_2 = Z_1 \cot\theta_2 \tag{19a}$$

$$Z_3 = Z_1 \frac{\cos^2\theta_2}{1 - 2\sin^2\theta_2} \tag{19b}$$

In order to have a compact equivalent T-shaped model, θ_2 should be less than 45^o (i.e. $2\theta_2 < \theta_1 = 90^o$). When Z_1 = 50 ohm, Fig. 47 plots the values of Z_2 and Z_3 versus θ_2 ($0^o < \theta_2 < 45^o$). When θ_2 is close to 45^o, Z_2 is approaching 50 ohm and Z_3 is going to infinity. The impedance looking into the shunt stub is $-jZ_3 \cot\theta_3 = \infty$. Therefore, at the T-junction, the shunt stub acts like an open circuit and could be neglected. Hence, as expected, the T-shaped transmission line model becomes a 90^o 50-ohm line, which is the original transmission line. Theoretically, there are numerous values of Z_2 and Z_3 satisfying (19). However, due to the limitations in the photolithography, etching ability, and circuit size, some combinations are impractical. Generally, for high impedance microstrip lines, low dielectric constant substrates are preferred to have practical narrow line width. For low impedance microstrip lines, high dielectric constant substrates are preferred to save circuit area.

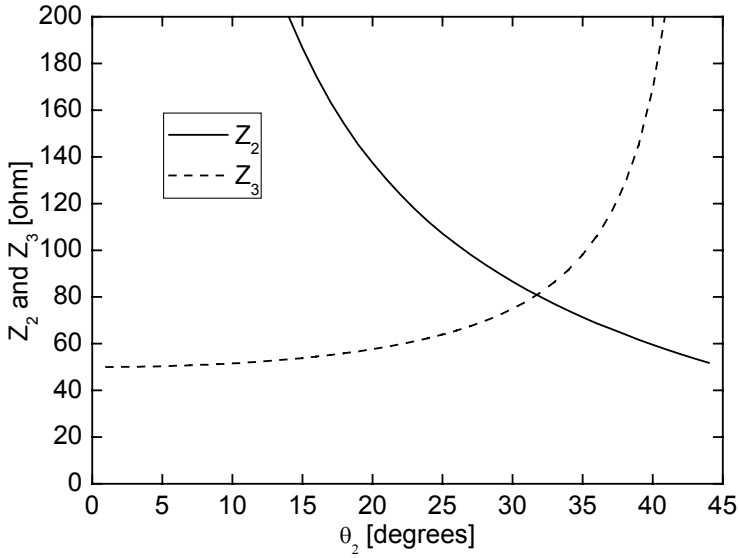

Fig. 47. Design curves for Z_2 and Z_3 vs. θ_2. ($Z_1 = 50$, $\theta_1 = 90^o$, and $\theta_3 = 45^o$)

To study how the equivalent T-shaped lines work, θ_2 is arbitrarily chosen as 30^o, and $Z_2 = 86.6$ ohm and $Z_3 = 75$ ohm. Fig. 48 plots the simulated results of the original connecting transmission line and the T-shaped transmission line at center frequency of 3 GHz. Since $Z_1 = 50$ ohm and $\theta_1 = 90^o$ (at 3 GHz), the simulated return loss of the original line is small. At 3 GHz, similar to the original line, the equivalent T-shaped line has a good impedance matching and a 90^o phase delay. In addition, it should be noted that at the second harmonic (6 GHz) the equivalent T-shaped line shows a transmission zero because of the shunt stub. The equivalent T-shaped line not only shows a compact size but also has the same characteristics as the original series 90^o line at passband and a transmission zero at the second harmonic which improves out-band rejection.

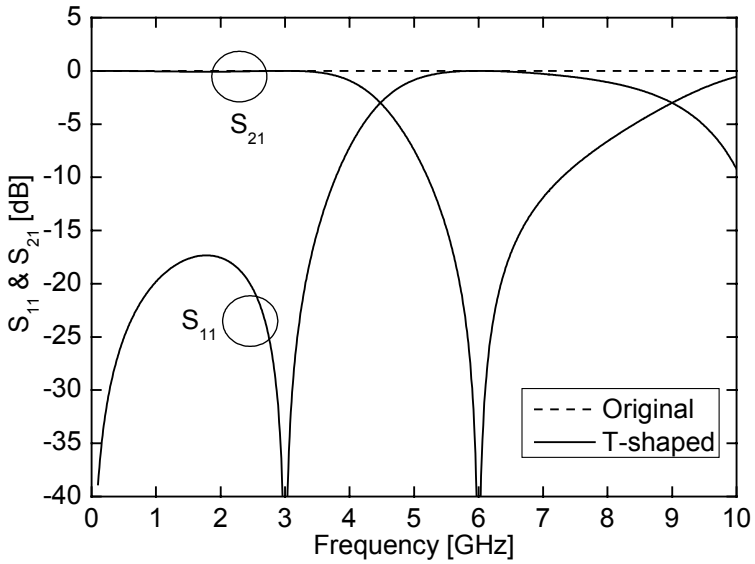

(a)

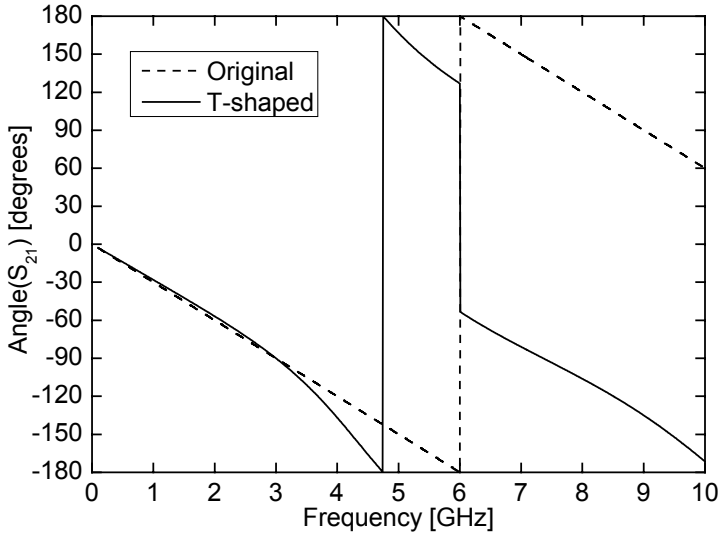

(b)

Fig. 48. Simulated results of the original 50-ohm 90^{o} connecting line and equivalent T-shaped line (center frequency = 3 GHz). (a) magnitude and (b) phase.

B. Integration of bandpass and bandstop filter

The equivalent T-shaped line could is then integrated into a conventional

half-wavelength open-stub bandpass filter for second harmonic rejection and a compact size. Fig. 49 shows a conventional 3-pole bandpass filter and the proposed filter. For a Chebyshev lowpass prototype filter with a passband ripple L_{Ar} = 0.1 dB, the element values are: $g_0 = 1$, $g_1 = 1.0316$, $g_2 = 1.1474$, $g_3 = 1.0316$, and $g_4 = 1$. With the fractional bandwidth $FBW = 0.3$, the parameters of the microstrip lines are: $Z_8 = 34$ ohm, $Z_9 = 17$ ohm, $Z_{10} = 37$ ohm, $\theta_8 = \theta_9 = 180^o$, and $\theta_{10} = 90^o$. When the filter center frequency = 3 GHz, Fig. 50 shows the simulated results of the conventional bandpass filter. Besides a passband at center frequency, it should be noted that there is another undesired passband at the 2nd harmonic (i.e. 6 GHz). To suppress the spurious passband, the two series connecting lines ($Z_{10} = 37$ ohm, $\theta_{10} = 90^o$) are then replaced by the equivalent T-shaped lines. Using the design equations (19a) and (19b), the parameters for the T-shaped lines are: $Z_{11} = 56$ ohm, $Z_{12} = 65$ ohm, $\theta_{11} = 45^o$, and $\theta_{12} = 30^o$.

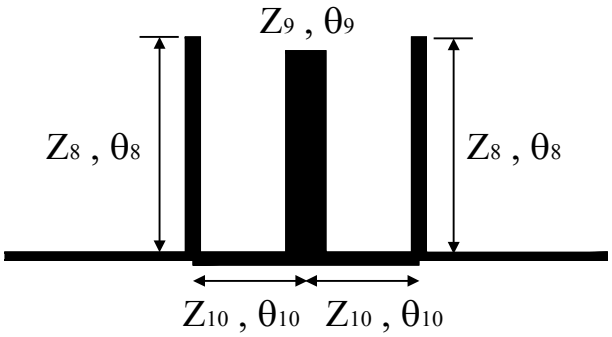

(a)

Fig. 49. Schematics of (a) conventional half-wavelength open-stub bandpass filter and (b) proposed bandpass filter.

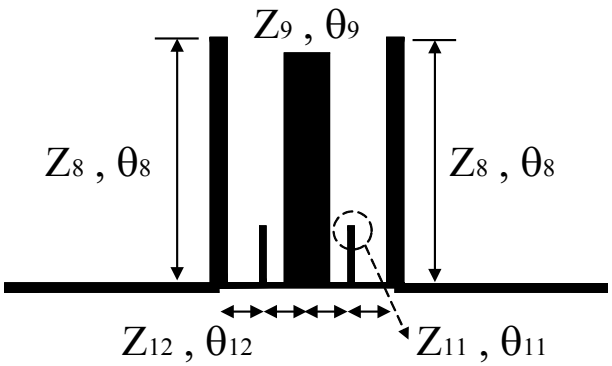

(b)

Fig. 49. Continued

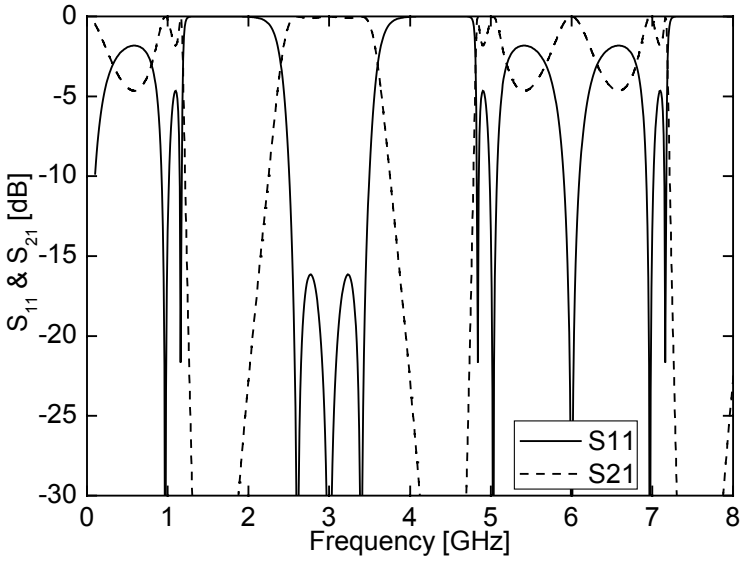

Fig. 50. Simulated results of conventional open-stub bandpass filter.

To validate the design concept, the two filters are built on 25-mil RT/Duroid 6010.8 (ε_r=10.8) substrate. The measured results are shown in Fig. 51. The two filters have similar passband response around 3 GHz. The insertion losses are all less than 1.4 dB, and the 10-dB return loss bandwidths are all 1.1 GHz. The center frequency of the

proposed filter increases by about 150 MHz (5%). This is due to that all the transmission lines are determined by transmission line model. Discontinuities such as open-end effects and T-junctions are not considered. At 6 GHz, the conventional filter shows a spurious passband. On the other hand, the proposed filter shows a 30-dB suppression on the undesired second harmonic at 6 GHz. Furthermore, the size of the conventional filter (excluding two feed lines) is 19.2 x 18.3 mm^2, while the size of the proposed filter (excluding two feed lines) is only 13.6 x 17.9 mm^2.

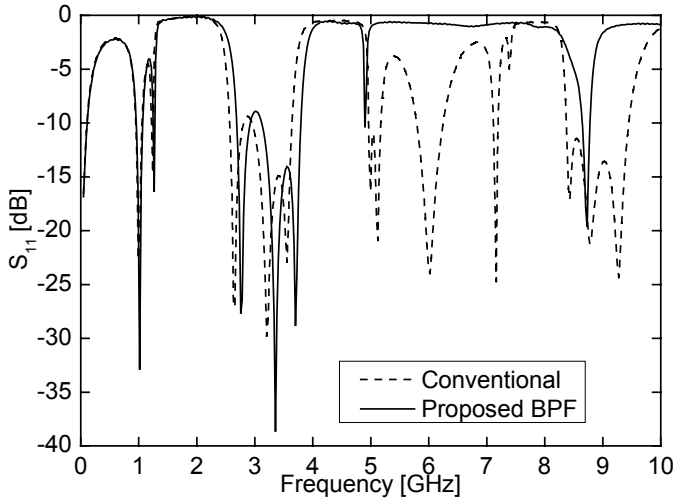

(a)

Fig. 51. Measured results of conventional and proposed bandpass filters. (a) return loss, (b) insertion loss, and (c) passband response.

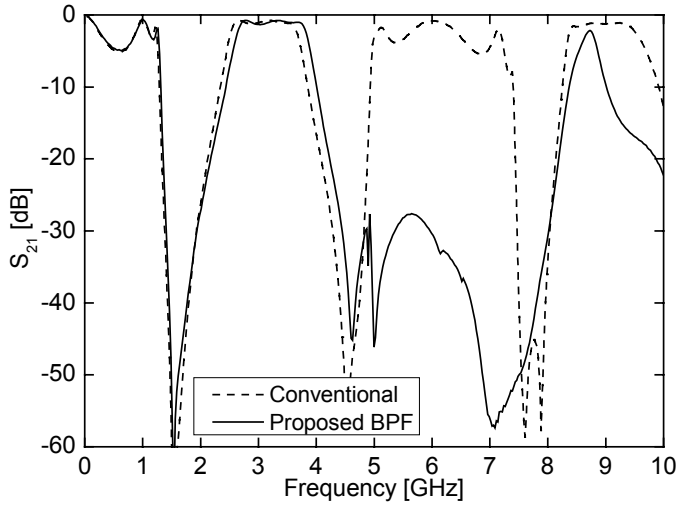

(b)

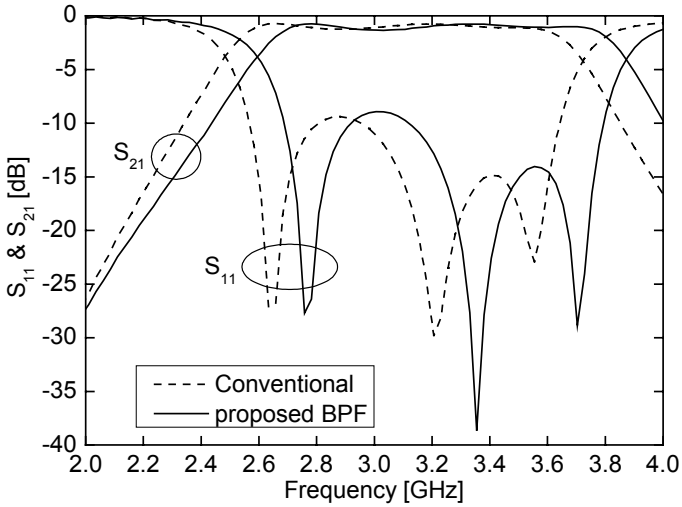

(c)

Fig. 51. Continued.

Fig. 52 shows the comparison of the measured results with the simulated results for the new filter. The simulation is carried out by IE3D[*]. The full-wave simulated results agree well with the measured results.

[*] IE3D version 10.2, Zeland Software Inc., Fremont, CA, 2004.

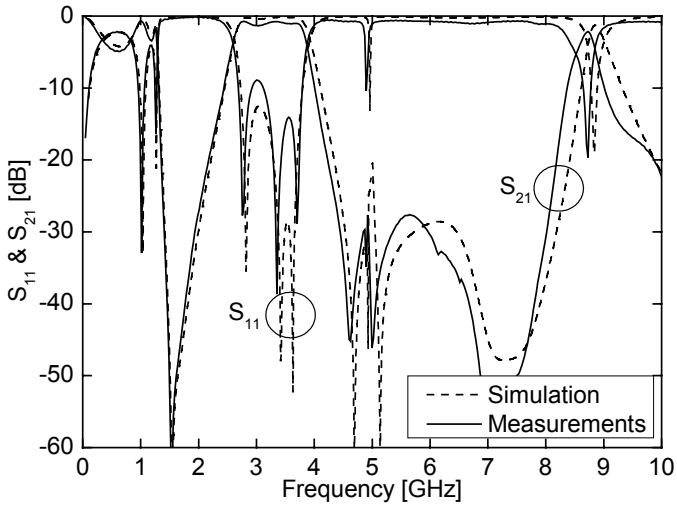

Fig. 52. Measured and full-wave simulated results of the proposed filter.

5.5 Conclusions

In this chapter, three conventional bandpass filters with spurious passbands are studied. The harmonic suppression is achieved by modifying the configurations of the filters instead of cascading additional bandstop filters or lowpass filters which increases the circuit sizes and the insertion loss in the passband.

A compact dual-mode bandpass filter with a square patch of the right crossed slots is investigated. The right crossed slots can lower the fundamental resonant frequency and keep the second resonant frequency unchanged. The proposed filter shows a 4.4 % fractional bandwidth at 1.595 GHz with a return loss of better than 10 dB and an insertion loss of less than 2.5 dB, while the second passband is located around 4.6 GHz = 2.88f_o, where f_o = 1.595 GHz. In addition, compared with conventional square patch filter of the same fundamental frequency, the proposed filter also shows a 58 % size

reduction.

Improved harmonic suppression for open-loop bandpass filter has been investigated. By adding the small shunt open stubs in the center of the resonators, improved upper stopband suppression is obtained. The suppression of 35 dB at the second harmonic is obtained. A design curve for determining the length of the stubs is derived using ABCD matrix calculation. Compared with the conventional filters, the modified filter shows improved suppression response with the same center passband response.

Design concept of the integrating bandstop filters into a bandpass filter has been investigated. With the requirement of second harmonic suppression without affecting the fundamental frequency response, the proposed filters not only have the advantage of compact size but also show good second harmonic suppression. The design concept has been validated through simulations and experiments. Over 30-dB improvement of the decond harmonic suppression and 28.6 % size reduction have been achieved.

CHAPTER VI

COMPACT MICROSTRIP BANDPASS FILTER USING SLOW-WAVE MULTI-SECTION STEPPED-IMPEDANCE RESONATOR

6.1 Introduction

The conventional uniform half-wavelength resonators are commonly used in bandpass filters such as end-coupled bandpass filters and parallel-coupled bandpass filters [19], [35]. These filters, however, occupy large circuit size, and the problem becomes even worse for low-frequency applications. Therefore, several methods were proposed for miniaturization. The length of a Combline resonator [47] is less than a quarter wavelength, however, the requirement of via holes and lumped capacitors not only increases the cost but also complicates the fabrication process, which makes the repeatability difficult to maintain. Stepped-impedance resonator has a compact length [37], but it requires a small impedance ratio between the low-impedance and high-impedance sections. In order to reduce the ratio and gain a compact length, the width of the low-impedance section is wide, and thus increases the overall resonator size. Slow-wave structures [48], [49] have shown promising results in size reduction. Besides, these resonators have a higher Q factor.

In this chapter, slow-wave multi-section stepped-impedance resonator and filter are studied. The resonator consists of sections of high-impedance and low-impedance

lines. As the line widths of the high-impedance lines decrease, the fundamental resonant frequency of the resonator decreases. Therefore, the proposed resonator has a compact size. A simple transmission-line model is used to analyze the resonator. The slow-wave structure is also used to design a 2-pole bandpass filter and a 3-pole bandpass filter.

6.2 Slow-wave multi-section stepped-impedance resonator

For a lossless transmission line, the phase velocity v_p is given by:

$$v_p = 1/\sqrt{LC} \tag{20}$$

where L is series inductance per unit length and C is the shunt capacitance per unit length. On the other hand, the wavelength λ is given by:

$$\lambda = v_p / f \tag{21}$$

where f is the frequency. Therefore, for a compact length transmission line, v_p should be small, and this could be obtained by either increasing series inductance L or shunt capacitance C. For microstrip lines, increasing L can be obtained by using a narrow (high-impedance) line and increasing C can be obtained by using a wide (low-impedance) line. In this study, increasing L is adopted due to that the wide lines (increasing C) occupy a large area and ruins the beauty of compactness of a slow-wave structure. Fig. 53(a) shows the conventional half-wavelength resonator and Fig. 53(b) shows the proposed slow-wave multi-section stepped-impedance resonator, which consists of seven sections.

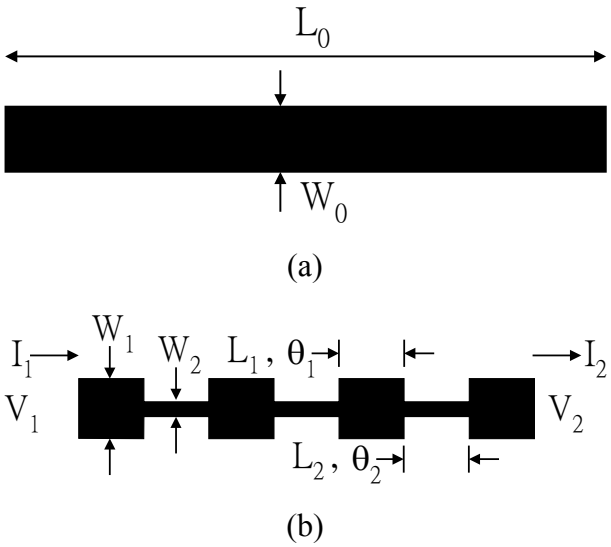

Fig. 53. Configurations of the resonators (a) conventional half-wavelength and (b) proposed slow-wave multi-section stepped-impedance.

In order not to increase resonator width, W_1 is equal to W_0, and only W_2 is decreased to obtain bigger series inductance L. To calculate the resonant frequency, a simple transmission-line model is used. The ABCD matrix of the slow-wave resonator is given by:

$$\begin{pmatrix} A & B \\ C & D \end{pmatrix}_T = M_{END} M_1 M_{STEP1} M_2 M_{STEP2} M_1 M_{STEP1} M_2 M_{STEP2} M_1 M_{STEP1} M_2 M_{STEP2} M_1 M_{END} \quad (22)$$

where

$$M_1 = \begin{pmatrix} \cos\theta_1 & jZ_1 \sin\theta_1 \\ jY_1 \sin\theta_1 & \cos\theta_1 \end{pmatrix}$$

$$M_2 = \begin{pmatrix} \cos\theta_2 & jZ_2 \sin\theta_2 \\ jY_2 \sin\theta_2 & \cos\theta_2 \end{pmatrix}$$

where M_{END} is the ABCD matrix of the open end effect, M_{STEP1} and M_{STEP2} are the

ABCD matrixes of step effects [19], $Z_i = 1/Y_i$ are the characteristic impedance and θ_i are the electrical lengths, i = 1, 2. The resonance occurs when the open-circuited boundary conditions at both ends are satisfied, which means that $I_1 = I_2 = 0$ A. Since $I_1 = C_T V_2 + D_T I_2$, C_T is equal to zero at resonance. The values of C_T can be plotted by using Matlab. For simplicity, the electric lengths θ_1 and θ_2 are set to be equal. Defining the impedance ratio $R = Z_2 / Z_1$, Fig. 54 plots the required electric lengths for resonance with different impedance ratio. When $R = 1$, $\theta_1 = \theta_2 = 25.7^o$. This is the conventional uniform resonator case because $4\theta_1 + 3\theta_2 = 180^o$. When R > 1, the resonator has a compact length because of $4\theta_1 + 3\theta_2 < 180^o$. When R < 1, the resonator also has a compact length, however, the resonator width is wider. Given $W_1 = W_0$, the width W_2 is greater than W_1 for $Z_2 < Z_1$, and the width of the resonator has a wider width in comparison with the conventional uniform resonator. Therefore, the case R < 1 is preferred for a compact resonator length without increasing the resonator width.

Table I summarizes several cases of the slow-wave resonators. The resonators are built on a 31-mil RT/Duroid 5880 substrate with the dielectric constant of 2.33. The resonant frequencies are measured with two coupling gap of 0.2 mm at both ends of the resonators. The simulated resonant frequency is 4 GHz, and the measured resonant frequencies show a good agreement of less 5 % difference. Given that the resonator widths are all equal to 2.5 mm, the total resonator lengths reduce from 26.95 mm of case 1 to 20.24 mm of case 6. The slow-wave resonator (case 6) shows a 25 % size reduction in comparison with the conventional uniform resonator (case 1).

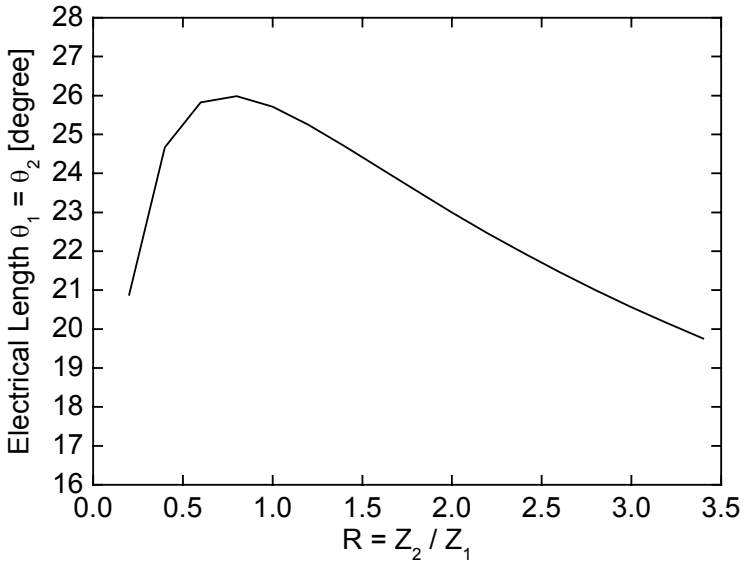

Fig. 54. Electric lengths vs. impedance ratio *R*.

Table 1. Summary of slow-wave resonators (W_1 and W_2 in mm, θ_1 and θ_2 in degrees)

	W_1	θ_1	W_2	θ_2	R	Length (mm)	Measured resonant frequency (GHz)
Case 1	2.5	25.6	2.5	25.6	1	26.95	3.91
Case 2	2.5	25.3	2	25.3	1.13	26.69	3.89
Case 3	2.5	24.7	1.5	24.7	1.35	25.85	3.88
Case 4	2.5	23.7	1	23.7	1.69	24.68	3.85
Case 5	2.5	22.0	0.5	22.0	2.31	22.5	3.86
Case 6	2.5	20.0	0.2	20.0	3.16	20.24	3.83

6.3 Filter design

A. Two-pole bandpass filter

The slow-wave multi-section stepped-impedance resonator is then used to build a 2-pole bandpass filter as shown in Fig. 55. Chebyshev response with the passband ripple

of 0.1 dB is selected (g_0 = 1, g_1 = 0.8431, g_2 = 0.622, g_3 = 1.3554). The fractional bandwidth (*FBW*) is 0.05, and the center frequency is 4 GHz. The gap (*g*) of 0.2 mm between the two resonators is used to have the coupling coefficient M = 0.069, where the coupling coefficient is given by [19]:

$$M = FBW \Big/ \sqrt{g_1 g_2} \tag{23}$$

The dimension of the resonator are W_1 = 2.5 mm, W_2 = 0.2 mm, $L_1 = L_2$ = 2.7 mm. The filter is directly connnected to the input and output microstrip lines to reduce coupling loss. In each line, a section of microstrip line of W_3 = 0.5 mm and L_3 = 4 mm is used for impedance matching. Fig. 56 shows the simulated and measured results. The simulation is carried out by an electromagnetic full-wave simulator IE3D*. From 3.97 to 4.23 GHz, the measured return loss is better than 10 dB and the insertion loss is less than 1.9 dB. The measurements agree well with the simulated results.

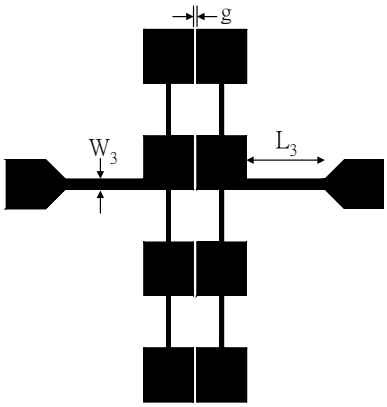

Fig. 55. Two-pole bandpass filter using slow-wave resonator.

* IE3D version 10.2, Zeland Software Inc., Fremont, CA, 2004.

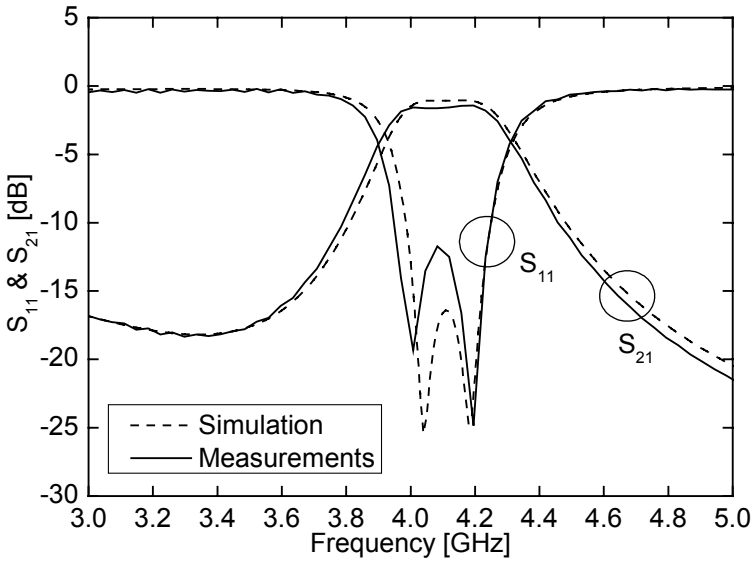

Fig. 56. Simulated and measured results of the two-pole bandpass filter.

B. Three-pole bandpass filter

The slow-wave resonator is further used to build a three-pole bandpass filter as shown in Fig. 57. For the two-pole bandpass filter, although the resonators have compact length, it is the two additional lines of W_3 = 0.5 mm and L_3 = 4 mm that ruin the compact beauty. To tackle this problem, a three-pole bandpass filter is investigated. Instead of tapped-line coupling, coupled-line coupling is used to eliminate the two additional lines. In order to increase the coupling between feed lines and the first and third resonators, the two resonators are modified. The thin lines are shifted toward the coupling lines, and the resonant frequency of the resonator shifts to a lower frequency. To compensate this effect, the thin line width L_2 of 0.2 mm (see Fig. 53) are changed to 0.33 mm. The rest dimensions of the resonators for the three-pole bandpass filter are the same with those of the two-pole bandpass filter.

Chebyshev response with the passband ripple of 0.1 dB is selected (g_0 = 1, g_1 = 1.0316, g_2 = 1.1474, g_3 = 1.0316, g_4 = 1). The fractional bandwidth (*FBW*) is 0.05, and the center frequency is 4 GHz. The gap of G_2 = 0.45 mm between the first-second resonators and second-third resonators is used to have the coupling coefficient M = 0.046, where the coupling coefficient is given by [19]:

$$M = FBW \Big/ \sqrt{g_1 g_2} \tag{24}$$

The coupled line of L_4 = 10.75 mm, W_4 = 0.7 mm, and G_1 = 0.4 mm is used to have the external quality factor $Q_{ext,i}$ = 20.63, i = 1, 2, where the external quality factor is given by [19]:

$$Q_{ext,1} = g_0 g_1 / FBW = g_3 g_4 / FBW = Q_{ext,2} \tag{25}$$

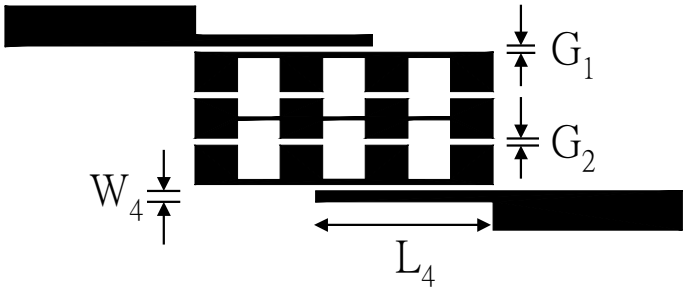

Fig. 57. Three-pole bandpass filter using slow-wave resonator.

Fig. 58 shows the measured and simulated results of the three-pole bandpass filter. The simulation is carried out by an electromagnetic full-wave simulator IE3D[*]. From 3.91 to 4.1 GHz, the measured return loss is better than 15 dB and the insertion loss is

[*] IE3D version 10.2, Zeland Software Inc., Fremont, CA, 2004.

less than 2.9 dB. The out-of-band rejection for the 3-pole filter is much better than that of the 2-pole filter. The measurements agree well with the simulated results.

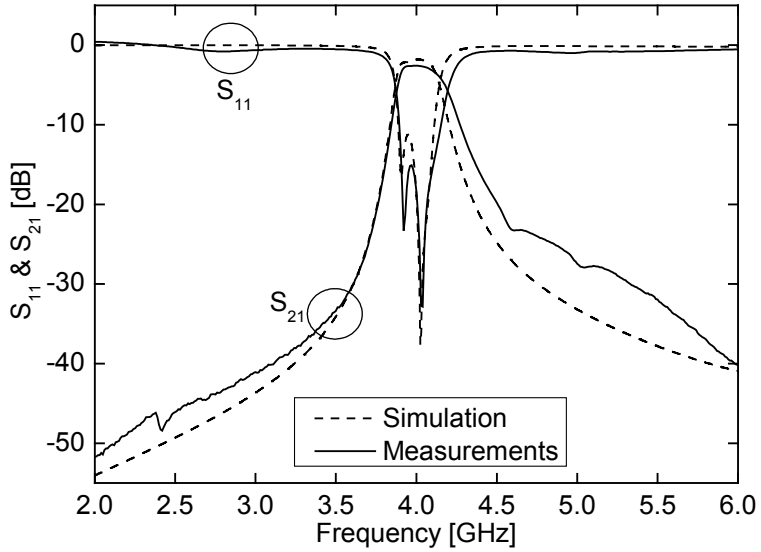

Fig. 58. Simulated and measured results of the three-pole bandpass filter.

6.4 Conclusions

Compact slow-wave multi-section stepped-impedance resonators are studied. Compared with the conventional uniform half-wavelength resonator, the slow-wave resonator shows a 25% size reduction. Applications such as bandpass filters are also included. The two-pole bandpass filter shows a measured return loss of better than 10 dB and an insertion loss of less than 1.9 dB from 3.97 to 4.23 GHz. For the three-pole bandpass filter, from 3.91 to 4.1 GHz, the measured return loss is better than 15 dB and the insertion loss is less than 2.9 dB.

CHAPTER VII

SUMMARY

In this dissertation, two wideband phased array antennas are studied. The lineraly polarized array antenna consists of a power divider, a PET-controlled phase shifter, and a Vivaldi antenna array. A wideband transition between a microstrip line and a slotline is investigated to feed the Vivaldi antenna. This array can operate from 3 to 12 GHz with a steering angle of $\pm 15^{o}$. For the X-band circularly polarized array antenna, a spiral antenna array is used.

Furthermore, several microtrip filters are proposed for harmonic suppression. In Chapter III, a compact bandstop filter using open stubs and a spurline is studied. The proposed bandstop filter shows a wider and a deeper rejection. The proposed filter is also used to suppress the second harmonic of an open-loop bandpass filter. In Chapter IV, two lowpass filters using distributed elements and slotted ground structures are introduced. Design methods, discussions, and comparisons of these two filters are outlined.

In Chapter V, three conventional badnpass filters are investigated for harmonic suppression. For the dual-mode patch bandpass filter, a right cross slot perturbs the fundamental current distribution and lowers the resonant frequency. Therefore, a wider upper stopband and a compact circuit are achieved. For the open-loop bandpass filter, two shunt open stubs are added to the centers of the two resonators. The shunt open stubs do not affect the fundamental resonant frequency of the open loop, but lower the

second resonant frequency of the open loop. Compared with the conventional filters, the modified filter shows improved harmonic suppression response with the same center passband response. For the open stub bandpass filter, a design concept of the integrating bandstop filters has been investigated. With the requirement of second harmonic suppression without affecting the fundamental frequency response, the proposed filters not only have the advantage of compact size but also show good second harmonic suppression. The design concept has been validated through simulations and experiments. Over 30-dB improvement of the second harmonic suppression and 28.6 % size reduction have been achieved.

In Chapter VI, compact slow-wave multi-section stepped-impedance resonators are introduced. Compared with the conventional uniform half-wavelength resonator, the slow-wave resonator shows a 25% size reduction. A simple transmission-line model is used to analyze the proposed resonator. The resonator is also used to build a two-pole and a three-pole bandpass filters.

Finally, the wideband phsed array antennas are suggested for future study on applications of short-pulse ultra-wideband (UWB) technology [50].

REFERENCES

[1] S. N. Prasad and S. Mahapatra, "A novel MIC slot-line antenna," in *1979 European Microwave Conference*, Brighton, England, Sept. 1979, pp. 120-124.

[2] P. J. Gibson, The Vivaldi aerial, in *1979 European Microwave Conference*, Brighton, England, Sept. 1979, pp. 101-105.

[3] K. S. Yngvesson, D. H. Schaubert, T. L. Korzeniowski, E. L. Kollberg, T. Thungren, and J. F. Johansson, "Endfire tapered slot antennas on dielectric substrates," *IEEE Trans. Antennas Propagat.*, vol. 33, no.12, pp. 1392-1400, Dec. 1985.

[4] W. Sorgel, C. Waldschmidt, and W. Wiesbeck, "Transient responses of a Vivaldi antenna and a logarithmic periodic dipole array for ultra wideband communication," in *IEEE Int. Antennas Propagat. Symp. Dig.,* Columbus, OH, June 2003, pp. 592-595

[5] J. D. Dyson, "The equiangular spiral antenna," *IRE Trans. Antennas Propagat.*, vol. 7, no. 2, pp. 181-187, Apr. 1959.

[6] M. Li, K. Tilley, J. McCleary, and K. Chang, "Broadband coplanar waveguide-coplanar strip-fed spiral antenna," *Electron. Lett*., vol. 31, no. 1, pp. 4-5, Jan. 1995.

[7] C. A. Balanis, *Antenna Theory* 2nd edition. New York: Wiley, 1997.

[8] D. E. Isbell, "Log periodic dipole arrays." *IRE Trans. Antennas Propagat*., vol. AP-8, pp. 260-267, May 1960.

[9] T.-Y. Yun and K. Chang, "Analysis and optimization of a phase shifter controlled by a piezoelectric transducer," *IEEE Trans. Microw. Theory Tech.*, vol. 50, no. 1, pp. 105-111, Jan. 2002.

[10] K. C. Gupta, R. Garg, and I. J. Bahl, *Microstrip Lines and Slotlines*, Norwood, MA: Artech House, 1979.

[11] D. M. Pozar, *Microwave Engineering*, New York: Wiley, 1998.

[12] D.H. Schaubert and J. Shin, "Parameter study of tapered slot antenna arrays," in *IEEE Int. Antennas Propagat. Symp. Dig*., Newport Beach, CA, June 1995, pp. 1376-1379.

[13] T.-Y. Yun and K. Chang, "A low-cost 8 to 26.5 GHz phased array antenna using a piezoelectric transducer controlled phased shifter," *IEEE Trans. Antennas Propagat.*, vol. 49, no. 9, pp. 1290-1298, Sept. 2001.

[14] S.-G. Kim and K. Chang, "A low cross-polarized antipodal Vivaldi antenna for wideband operation," in *IEEE Int. Antennas Propagat. Symp. Dig.,* Monterey, CA, June, 2004, pp. 2269-2272.

[15] S.-G. Kim and K. Chang, "Ultrawide-band transitions and new microwave components using double-sided parallel-strip lines," *IEEE Trans. Microw. Theory Tech.*, vol. 52, no. 9, pp. 2148-2152, Sept. 2004.

[16] V. Radisic, M. Micovic, M. Hu, P. Janke, C. Ngo, L. Nguyen, L. Samoska, and M. Morgan, "164-GHz MMIC HEMT doubler," *IEEE Microw. Wireless Compon. Lett.*, vol. 11, no. 6, pp. 241-243, June 2001.

[17] B. Strassner and K. Chang, "Wide-band low-loss high-isolation microstrip periodic-stub diplexer for multiple-frequency applications," *IEEE Trans. Microw. Theory Tech*., vol. 49, no. 10, pp. 1818-1820, Oct. 2001.

[18] C. Quendo, E. Rius, and C. Person, "Narrow bandpass filters using dual-behavior resonators, " *IEEE Trans. Microw. Theory Tech.*, vol. 51, no. 3, pp. 734-743, Mar. 2003.

[19] J.-S. Hong and M. J. Lancaster, *Microstrip Filters for RF/Microwave Applications*. New York: Wiley, 2001.

[20] R. N. Bates, "Design of microstrip spurline bandstop filters," *IEE Journal of Microw., Optics, Acoustics*, vol. 1, no. 6, pp. 209-214, Nov. 1977.

[21] C. Nguyen and K. Chang, "On the analysis and design of spurline bandstop filters," *IEEE Trans. Microw. Theory Tech.*, vol. 33, no. 12, pp. 1416-1421, Dec. 1985.

[22] J.-S. Hong and M. J. Lancaster, "Couplings of microstrip square open-loop resonators for cross-coupling planar microwave filters," *IEEE Trans. Microw. Theory Tech.,* vol. 44, no. 12, pp. 2099-2109, Dec. 1996.

[23] L.-H. Hsieh and K. Chang, "Tunable microstrip bandpass filters with two transmission zeros," *IEEE Trans. Microw. Theory Tech*., vol. 51, no. 2, pp. 520-525, Feb. 2003.

[24] J.-W. Sheen, "A compact semi-lumped low-pass filter for harmonics and spurious suppression," *IEEE Microw. Wireless Compon. Lett.*, vol. 10, no. 3, pp. 92-93, Mar. 2000.

[25] Y.-W. Lee, S.-M. Cho, G.-Y. Kim, J.-S. Park, D. Ahn, and J.-B. Lim, "A design of the harmonic rejection coupled line low-pass filter with attenuation poles," in *IEEE MTT-S Int. Microw. Symp. Dig.,* 1999, pp. 682-685.

[26] L.-H. Hsieh and K. Chang, "Compact elliptic-function low-pass filters using microstrip stepped-impedance hairpin resonators," *IEEE Trans. Microw. Theory Tech.*, vol. 51, no. 1, pp. 193-199, Jan. 2003.

[27] W.-H. Tu and K. Chang, "Compact microstrip low-pass filter with sharp rejection," *IEEE Microw. Wireless Compon. Lett.*, vol. 15, no. 6, pp. 404-406, June 2005.

[28] D. Ahn, J.S. Park, C.S. Kim, J. Kim, Y. Qian, and T. Itoh, "A design of the low-pass filter using the novel microstrip defected ground structure," *IEEE Trans. Microw. Theory Tech.*, vol. 49, no. 1, pp. 86-93, Jan. 2001.

[29] J.S. Lim, C.S. Kim, D. Ahn, Y.C. Jeong, and S. Nam, "Design of low-pass filters using defected ground structure," *IEEE Trans. Microw. Theory Tech.*, vol. 53, no. 8, pp. 2539-2545, Aug. 2005.

[30] G. Gonzales, *Microwave Transistors Amplifiers Analysis and Design*. Englewood Cliffs, NJ: Prentice Hall, 1996.

[31] R. R. Mansour, "Design of superconductive multiplexers using single-mode and dual-mode filters," *IEEE Trans. Microw. Theory Tech.*, vol. 42, no. 7, pp. 1411-1418, July 1994.

[32] L. Zhu, P.-M. Wecowski, and K. Wu, "New planar dual-mode filter using cross-slotted patch resonator for simultaneous size and loss reduction," *IEEE Trans. Microw. Theory Tech.*, vol. 47, no. 5, pp. 650-654, May 1999.

[33] L. Zhu, B. C. Tan, and S. J. Quek, "Miniaturized dual-mode bandpass filter using inductively loaded cross-slotted patch resonator," *IEEE Microw. Wireless Compon. Lett.*, vol. 15, no. 1, pp. 22-24, Jan. 2005.

[34] B. T. Tan, S. T. Chew, M. S. Leong, and B. L. Ooi, "A modified microstrip circular patch resonator filter," *IEEE Microw. Wireless Compon Lett*., vol. 12, no. 7, pp. 252-254, July 2002.

[35] G. L. Matthaei, L. Young, and E. M. T. Jones, *Microwave Filters, Impedance-Matching Networks, and Coupling Structures*. New York: McGraw-Hill, 1980.

[36] S. Cohn, "Parallel-coupled transmission-line resonator filters," *IRE Trans. Microw. Theory Tech*., vol. 6, pp. 223-231, April 1958.

[37] M. Makimoto, and S. Yamashita, "Bandpass filters using parallel coupled stripline stepped impedance resonators," *IEEE Trans. Microw. Theory Tech*., no. 12, pp. 1413-1417, Dec. 1980.

[38] J.-T. Kuo and E. Shih, "Microstrip stepped impedance resonator bandpass filter with an extended optimal rejection bandwidth," *IEEE Trans. Microw. Theory Tech*., no. 5, pp. 1554-1559, May 2003.

[39] Y. W. Kong and S. T. Chew, "EBG-based dual mode resonator filter," *IEEE Microw. Wireless Comp. Lett.*, vol. 14, no. 3, pp. 124-126, Mar. 2004.

[40] J.-R. Lee, J.-H. Cho, and S.-W. Yun, “New compact bandpass filter using microstrip λ/4 resonators with open stub inverter,” *IEEE Microw. Guided Wave Lett.,* vol. 10, no. 12, pp.526-527, Dec. 2000.

[41] L. Zhu and W. Menzel, “Compact microstrip bandpass filter with two transmission zeros using a stub-tapped half-wavelength line resonator,” *IEEE Microw. Wireless Comp. Lett*., vol. 13, no. 1, pp. 16-18, Jan. 2003.

[42] J.-T. Kuo, W.-H. Hsu, and W.T. Huang, “Parallel coupled microstrip filters with suppression of harmonic response,” *IEEE Microw. Wireless Comp. Lett*., vol. 12, no. 10, pp. 383-385, Oct. 2002.

[43] T. Lopetegi, M.A.G. Laso, J. Hernandez, M. Bacaicoa, D. Benito, M.J. Garde, M. Sorolla, and M. Guglielmi, “New microstrip ‘wiggly-line’ filters with spurious passband suppression,” *IEEE Trans. Microw. Theory Tech*., vol. 49, no. 9, pp. 1593-1598, Sept. 2001.

[44] L. G. Maloratsky, “Improved BPF performance with wiggly coupled lines,” *Microwave & RF*, pp. 53-62, Apr. 2002.

[45] C. Quendo, E. Rius, C. Person, and M. Ney, "Integration of optimized low-pass filters in a bandpass filter for out-of-band improvement," *IEEE Trans. Microw. Theory Tech.*, vol. 49, no. 12, pp. 2376-2383, Dec. 2001.

[46] A. Manchec, C. Quendo, E. Rius, C. Person, and J.-F. Favennec, "Synthesis of dual behavior resonstor (DBR) filters with integrated low-pass structures for spurious responses suppression," *IEEE Microw. Wireless Compon. Lett.*, vol. 16, no. 1, pp. 4-6, Jan. 2006.

[47] S. Caspi and J. Adelman, “Design of combline and interdigital filters with tapped-line input,” *IEEE Trans. Microw. Theory Tech.*, vol. 36, no. 4, pp. 759-763, Apr. 1988.

[48] J.-S. Hong, and M.J. Lancaster, “Edge-coupled microstrip loop resonators with capacitive loading,” *IEEE Microw. Guided Wave Lett.*, vol. 5, no. 3, pp. 87-89,

Mar. 1995.

[49] J.-S. Hong, and M.J. Lancaster, "Capacitively loaded microstrip loop resonator," *Electron. Lett.*, vol. 30, no. 18, pp. 1494-1495, Sept. 1994.

[50] R. J. Fontana, "Recent system applications of short-pulse ultra-wideband (UWB) technology," *IEEE Trans. Microw. Theory Tech.*, vol. 52, no. 9, pp. 2087-2104, Sept. 2004.

VITA

Wen-Hua Tu was born in Chia-yi, Taiwan, R.O.C. in May 1977. In June of 1999, he received a Bachelor of Science degree in communication engineering from National Chiao Tung University, Hsinchu, Taiwan, R.O.C. In June of 2001, he received a Master of Science degree in communication engineering from National Taiwan University, Taipei, Taiwan, R.O.C. From Oct. of 2001 to June of 2003, he was in military service as a second lieutenant of communication engineering. Since Sept. 2003, Mr. Tu has been employed as a research assistant in the Electromagnetics and Microwave Laboratory at Texas A&M University under the direction of Dr. Kai Chang. His research interests include wideband phased array antennas, microwave oscillators, planar microwave filters, and microwave power transmission. Wen-Hua's address is: 4Fl., No. 7-3, Lane 88, Bade St., Shinjuang, Taipei, Taiwan, 24265.